Supplementary Information for

Electrostatically tuning radical addition and atom abstraction reactions with distonic radical ions

Oisin J. Shiels[a] and Samuel C. Brydon,[b] Berwyck L. J. Poad,[b] David L. Marshall,[b] Sevan D. Houston,[c] Hui Xing,[c] Paul V. Bernhardt,[c] G. Paul Savage,[d] Craig M. Williams,[c] David G. Harman,[e] Benjamin B. Kirk,[f] Gabriel da Silva,[g] Stephen J. Blanksby,*[b] and Adam J. Trevitt*[a]

[a]Molecular Horizons and School of Chemistry and Molecular Bioscience, University of Wollongong, Wollongong, New South Wales 2522, Australia

[b]Central Analytical Research Facility and School of Chemistry and Physics, Queensland University of Technology, Brisbane, Queensland 4001, Australia

[c]School of Chemistry and Molecular Biosciences, University of Queensland, Brisbane, 4072, Queensland

[d]CSIRO Manufacturing, Ian Wark Laboratory, Melbourne, 3168, Victoria, Australia.

[e]School of Medicine, Western Sydney University, Penrith, New South Wales 2751, Australia

[f]RKF Engineering Services, Wollongong NSW, 2500

[g]Department of Chemical Engineering, The University of Melbourne, Parkville, Victoria 3010, Australia

E-mail: adamt@uow.edu.au

stephen.blanksby@qut.edu.au

Phone: +61 2 4221 5545

Phone: +61 7 3138 3343

Table of Contents

Reference Mass Spectra and Kinetic Profiles

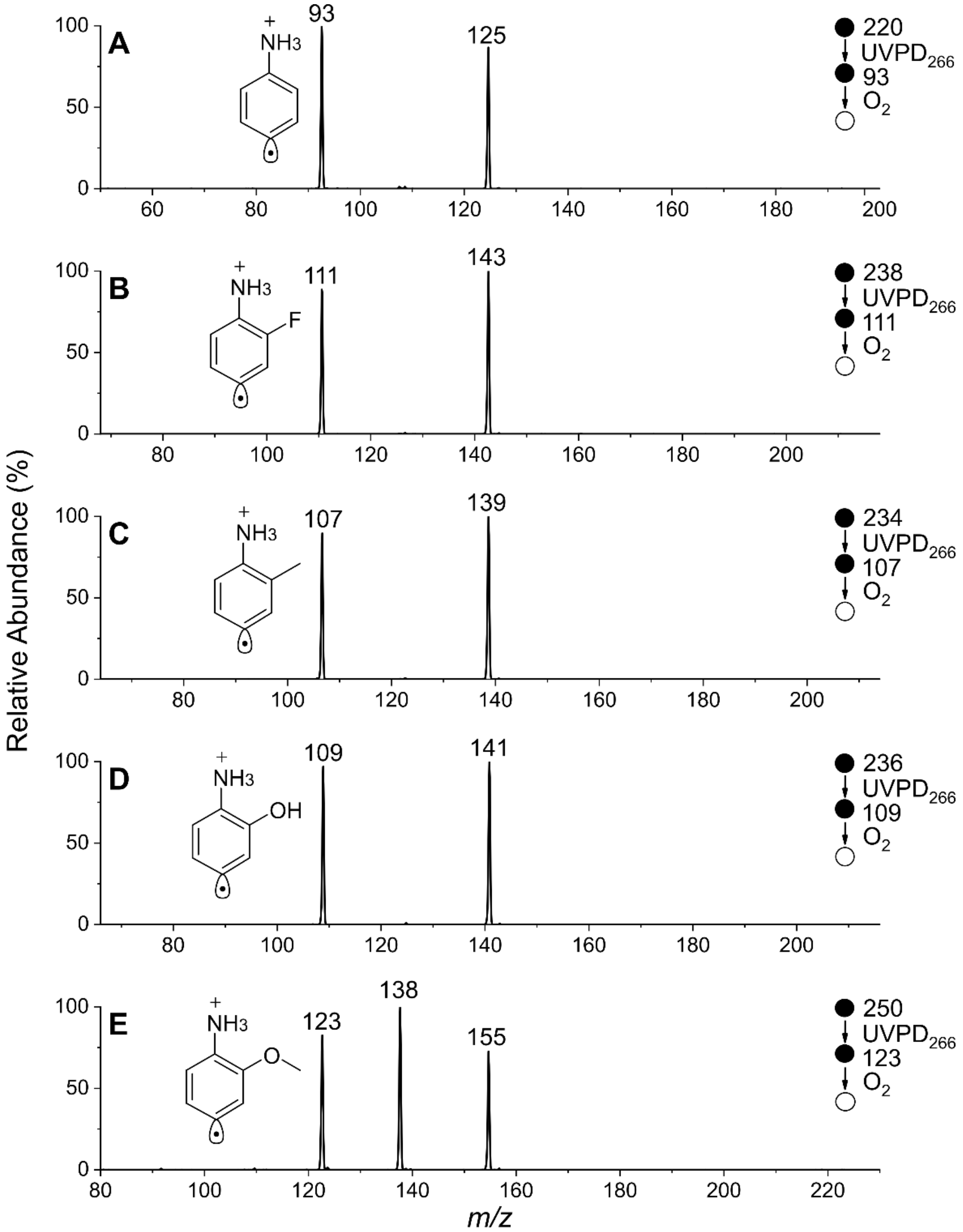

Figure S1. Representative MS^3 mass spectra for distonic radical oxidation reaction between 2-substituted 4-dehydroanilinium distonic radical cations and O_2 after 400 ms of reaction time, except for (D) which is after 200 ms of reaction time. **(A)** 4-dehydroanilinium ion (*m/z* 93) and the dioxygen adduct (*m/z* 125); **(B)** 2-fluoro-4-dehydroanilinium ion (*m/z* 111) and the dioxygen adduct (*m/z* 143); **(C)** 2-methyl-4-dehydroanilinium ion (*m/z* 107) and the dioxygen adduct (*m/z* 139); **(D)** 2-hydroxy-4-dehydroanilinium ion (*m/z* 109) and the dioxygen adduct (*m/z* 141); **(E)** 2-methoxy-4-dehydroanilinium ion (*m/z* 123) and the dioxygen adduct (*m/z* 155) followed by loss of a hydroxyl radical (*m/z* 138). Note that the experiments for (D) were run on a different day and the change in background [O_2] corrected for using the 4-dehydroanilinium radical cation (*m/z* 93) reaction with oxygen as a reference.

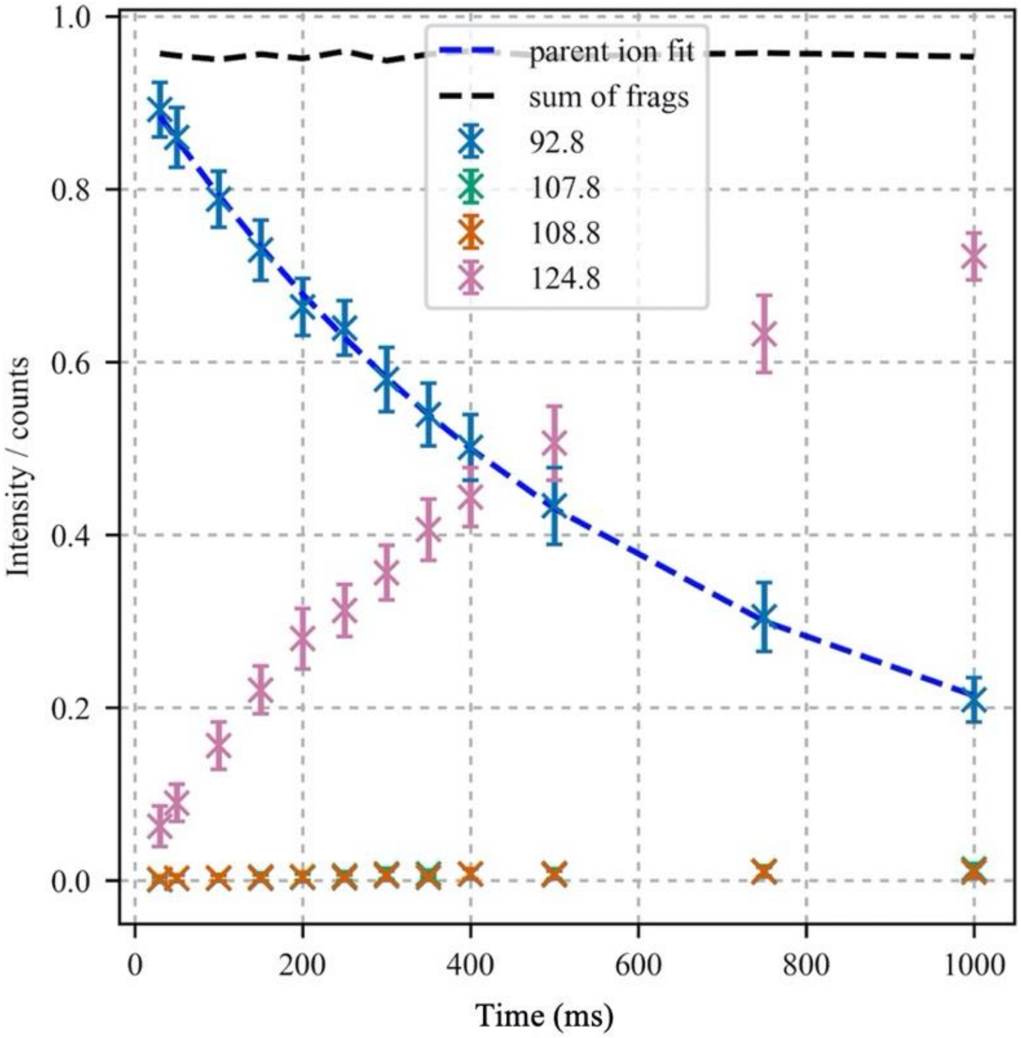

Figure S2. Kinetic profiles for the 4-dehydroanilinium cation (*m/z* 93) + O_2 reaction to give the major dioxygen adduct (*m/z* 125). These data were acquired in an MS^3 experiment following mass-selection of the radical cation, which was allowed to react with background oxygen in the linear quadrupole ion-trap, as depicted in Figure S1A.

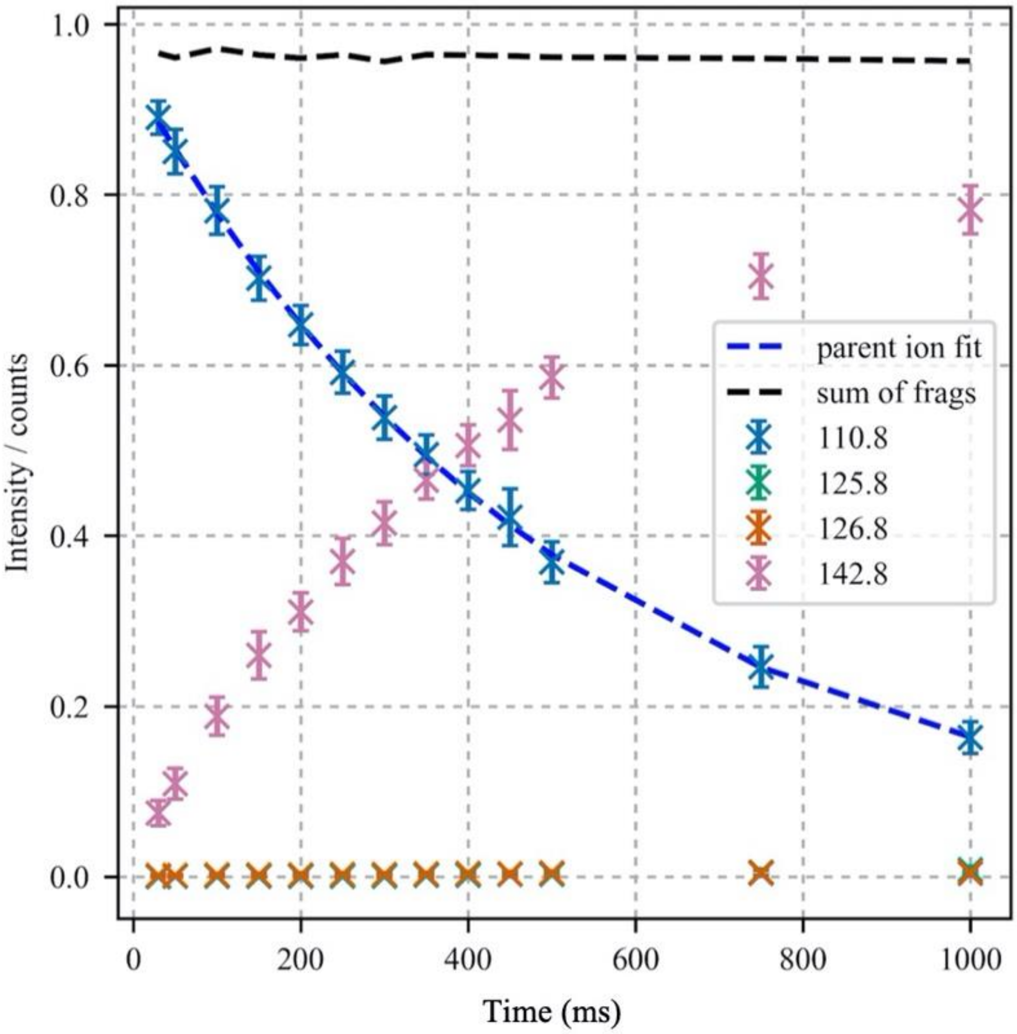

Figure S3. Kinetic profiles for the 2-fluoro-4-dehydroanilinium cation (*m/z* 111) + O_2 reaction to give the major dioxygen adduct (*m/z* 143). These data were acquired in an MS^3 experiment following mass-selection of the radical cation, which was allowed to react with background oxygen in the linear quadrupole ion-trap, as depicted in Figure S1B.

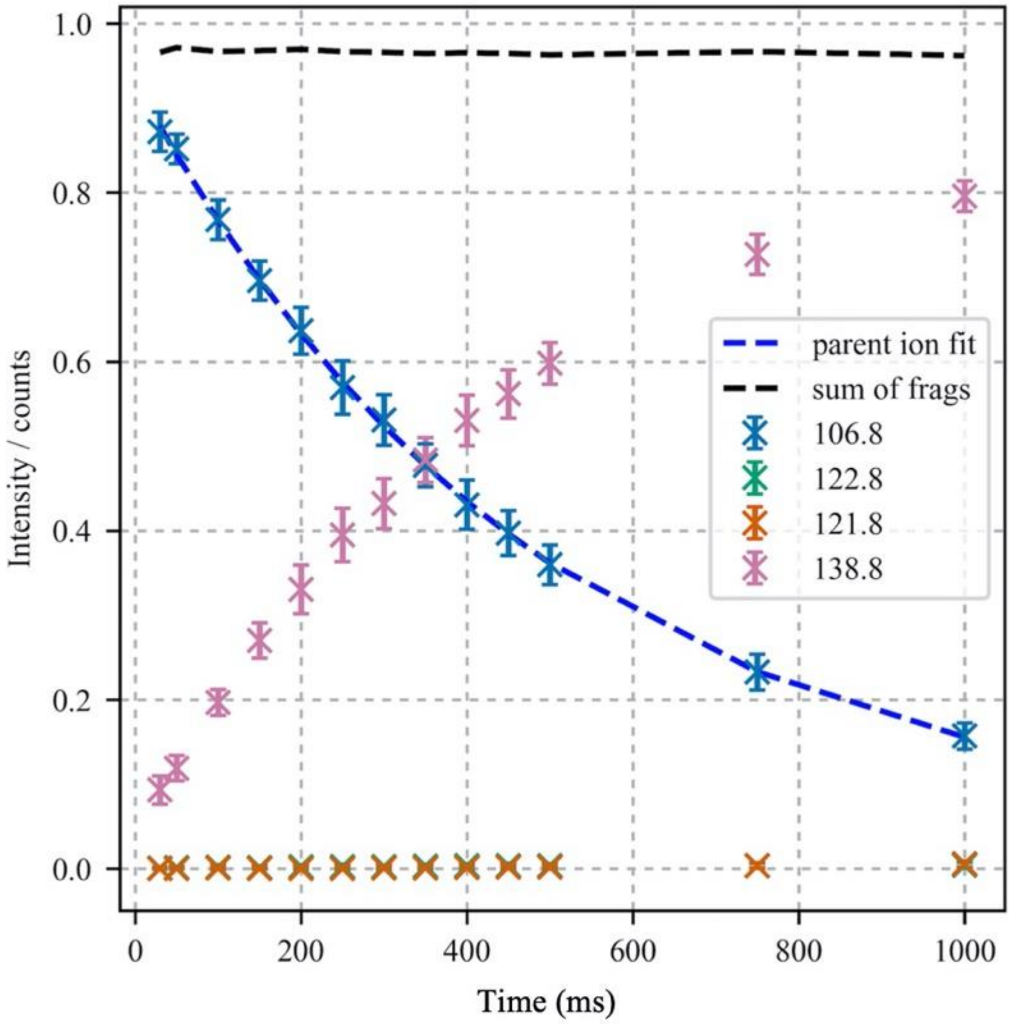

Figure S4. Kinetic profiles for the 2-methyl-4-dehydroanilinium cation (*m/z* 107) + O_2 reaction to give the major dioxygen adduct (*m/z* 139). These data were acquired in an MS^3 experiment following mass-selection of the radical cation, which was allowed to react with background oxygen in the linear quadrupole ion-trap, as depicted in Figure S1C.

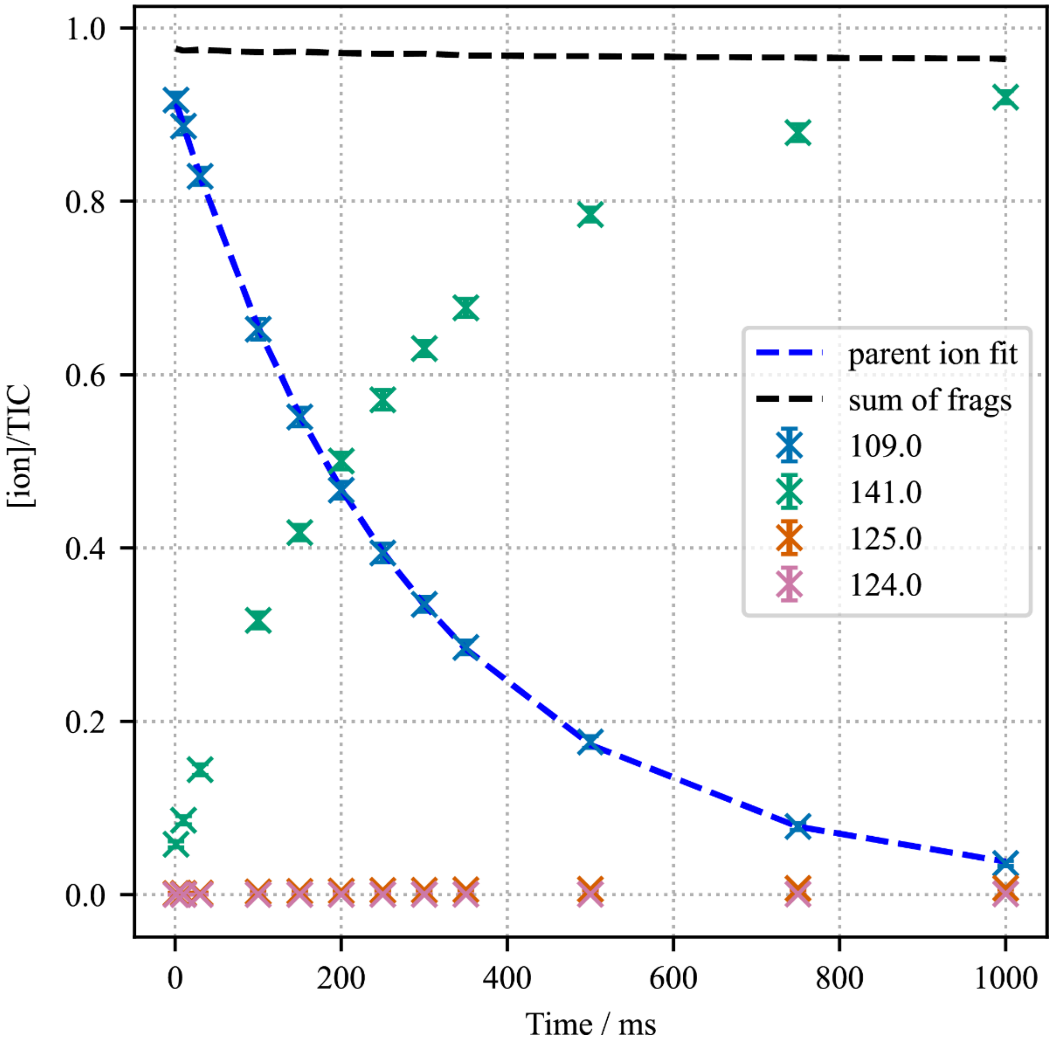

Figure S5. Kinetic profiles for the 2-hydroxy-4-dehydroanilinium cation (*m/z* 109) + O_2 reaction to give the major dioxygen adduct (*m/z* 141). These data were acquired in an MS^3 experiment following mass-selection of the radical cation, which was allowed to react with background oxygen in the linear quadrupole ion-trap, as depicted in Figure S1D.

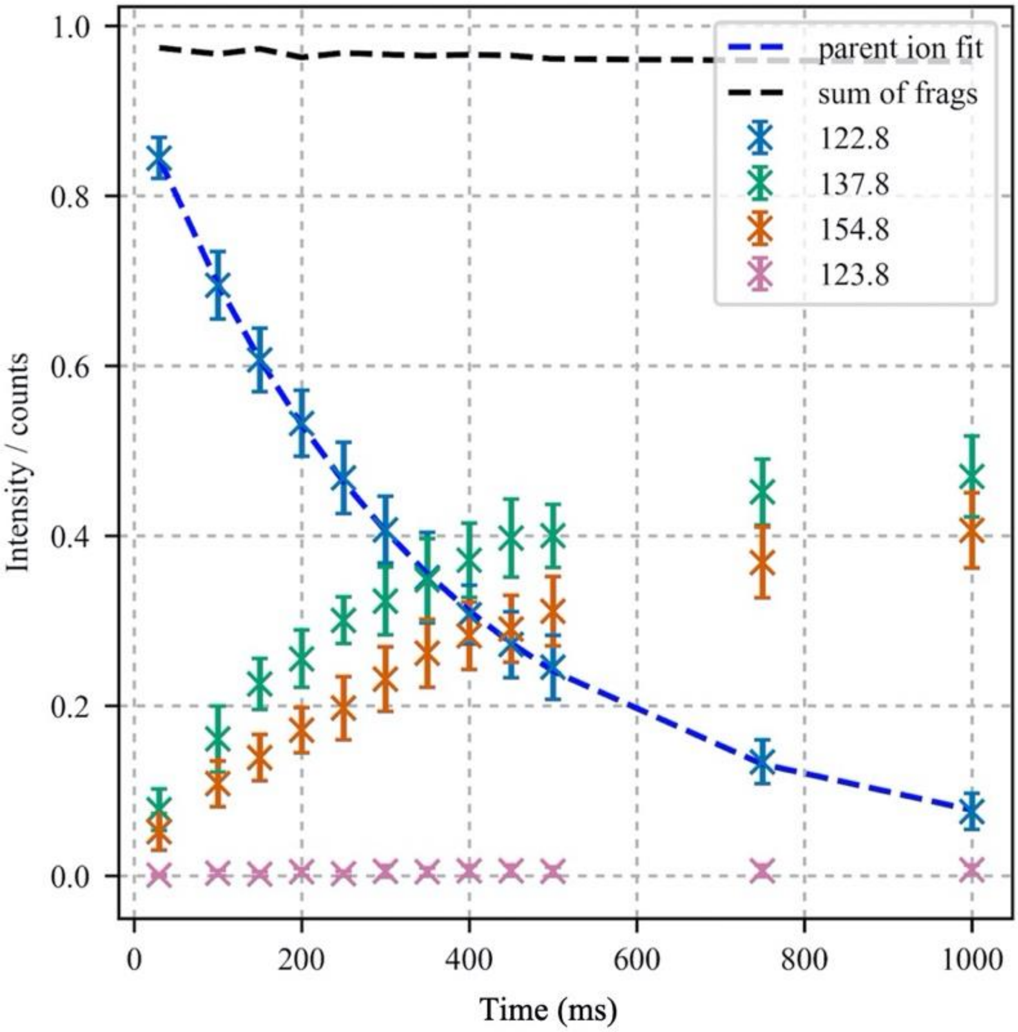

Figure S6. Kinetic profiles for the 2-methoxy-4-dehydroanilinium cation (*m/z* 123) + O_2 reaction to give the major dioxygen adduct (*m/z* 155) and subsequent loss of a hydroxyl radical (*m/z* 138) . These data were acquired in an MS^3 experiment following mass-selection of the radical cation, which was allowed to react with background oxygen in the linear quadrupole ion-trap, as depicted in Figure S1E.

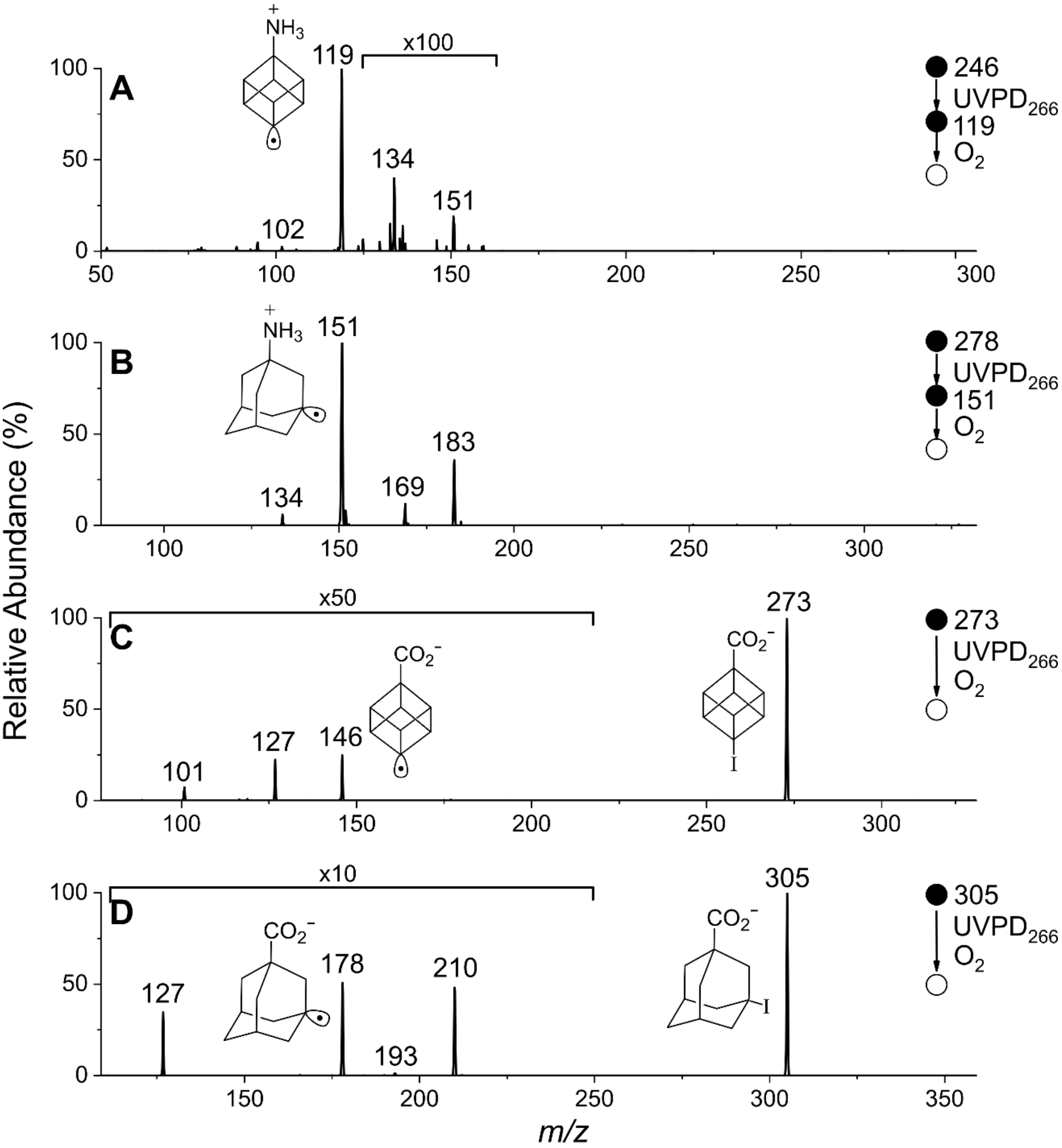

Figure S7. Representative mass spectra for distonic radical oxidation reaction between non-conjugated distonic radical ions and O_2. **(A)** MS^3 mass spectrum of 4-dehydrocubylammonium cation (*m/z* 119) and the dioxygen adduct (*m/z* 151) followed by loss of a hydroxyl radical (*m/z* 134) after 10,000 ms of reaction time, and other fragmentation pathways including loss of ammonia (*m/z* 102); **(B)** MS^3 mass spectrum of 3-dehydroadamantylammonium cation (*m/z* 151) and the dioxygen adduct (*m/z* 183) after 10,000 ms of reaction time, along with potential reaction with background water (*m/z* 169) and loss of ammonia (*m/z* 134); **(C)** MS^2 mass spectrum of 4-dehydrocubylcarboxylate anion (*m/z* 146) after 100 ms of reaction time, following photodissociation of 4-iodocubylcarboxylate anion (*m/z* 273) which also generates an iodide anion (*m/z* 127) and a $C_8H_5^-$ anion (*m/z* 101) following decarboxylation; **(D)** MS^2 mass spectrum of 3-dehydroadamantylcarboxylate anion (*m/z* 178) and the dioxygen adduct (*m/z* 210) followed by loss of a hydroxyl radical (*m/z* 193) after 100 ms of reaction time, following photodissociation of 3-iodoadamantylcarboxylate anion (*m/z* 305) which also generates an iodide anion (*m/z* 127). Note that (A) and (B) were run under lower $[O_2]$ conditions to (C) and (D).

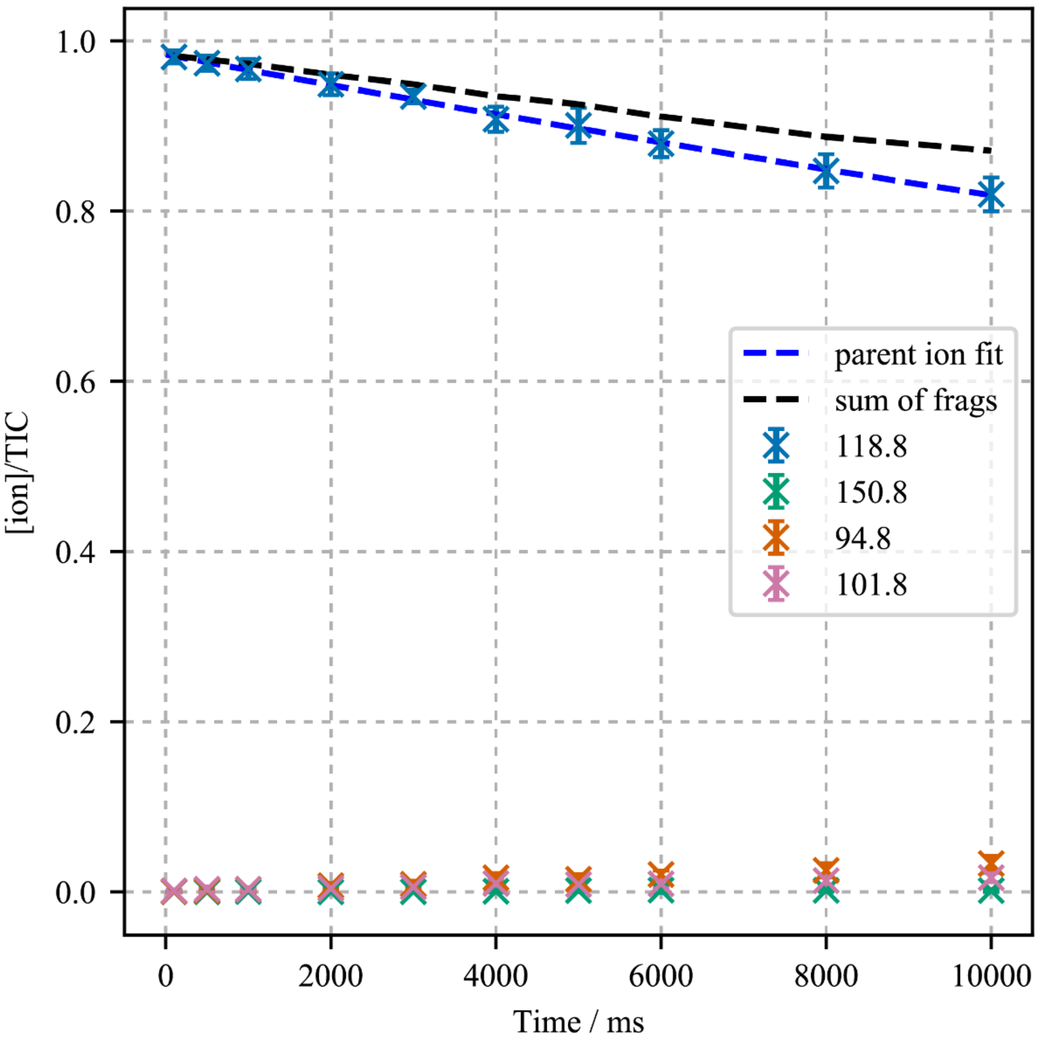

Figure S8. Kinetic profiles for the 4-dehydrocubylammonium cation (*m/z* 119) + O_2 reaction to give a minor dioxygen adduct (*m/z* 151) amongst other fragmentation pathways such as loss of ammonia (*m/z* 102). These data were acquired in an MS^3 experiment following mass-selection of the radical cation, which was allowed to react with background oxygen in the linear quadrupole ion-trap, as depicted in Figure S7A.

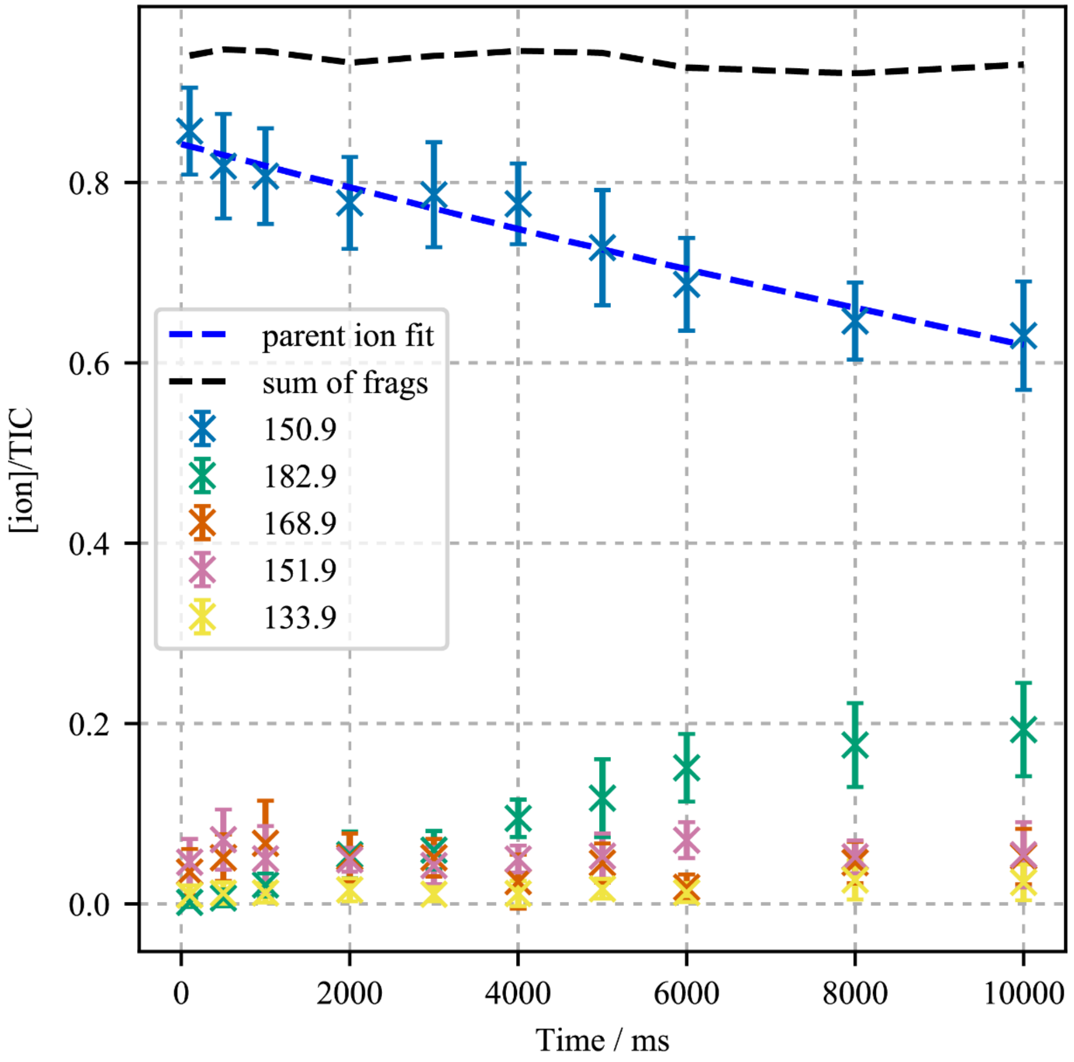

Figure S9. Kinetic profiles for the 3-dehydroadamantylammonium cation (*m/z* 151) + O_2 reaction to generate the dioxygen adduct (*m/z* 183), along with potential reaction with background water (*m/z* 169, noting this product does not increase in abundance with reaction time) and loss of ammonia (*m/z* 134). These data were acquired in an MS^3 experiment following mass-selection of the radical cation, which was allowed to react with background oxygen in the linear quadrupole ion-trap, as depicted in Figure S7B.

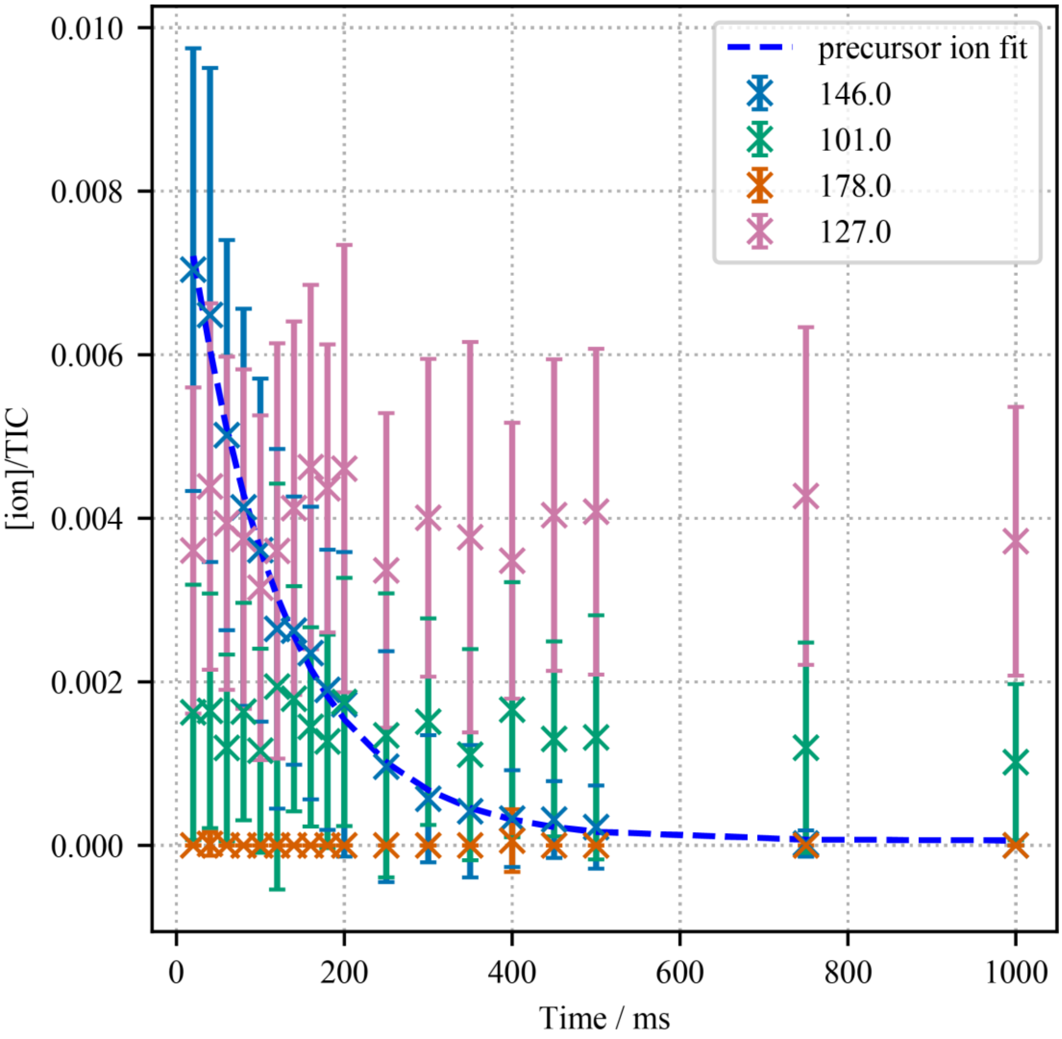

Figure S10. Kinetic profiles for the 4-dehydrocubylcarboxylate anion (*m/z* 273) + O_2 reaction. These data were acquired in an MS^2 experiment where radical anions were generated by photodissociation and allowed to react with oxygen in the linear quadrupole ion-trap without re-isolation, as depicted in Figure S7C. Decay of the reactant and evolution of product ions is normalised to the abundance of the unreactive iodide anion (*m/z* 127) formed in the photodissociation event to account for a loss of charge.

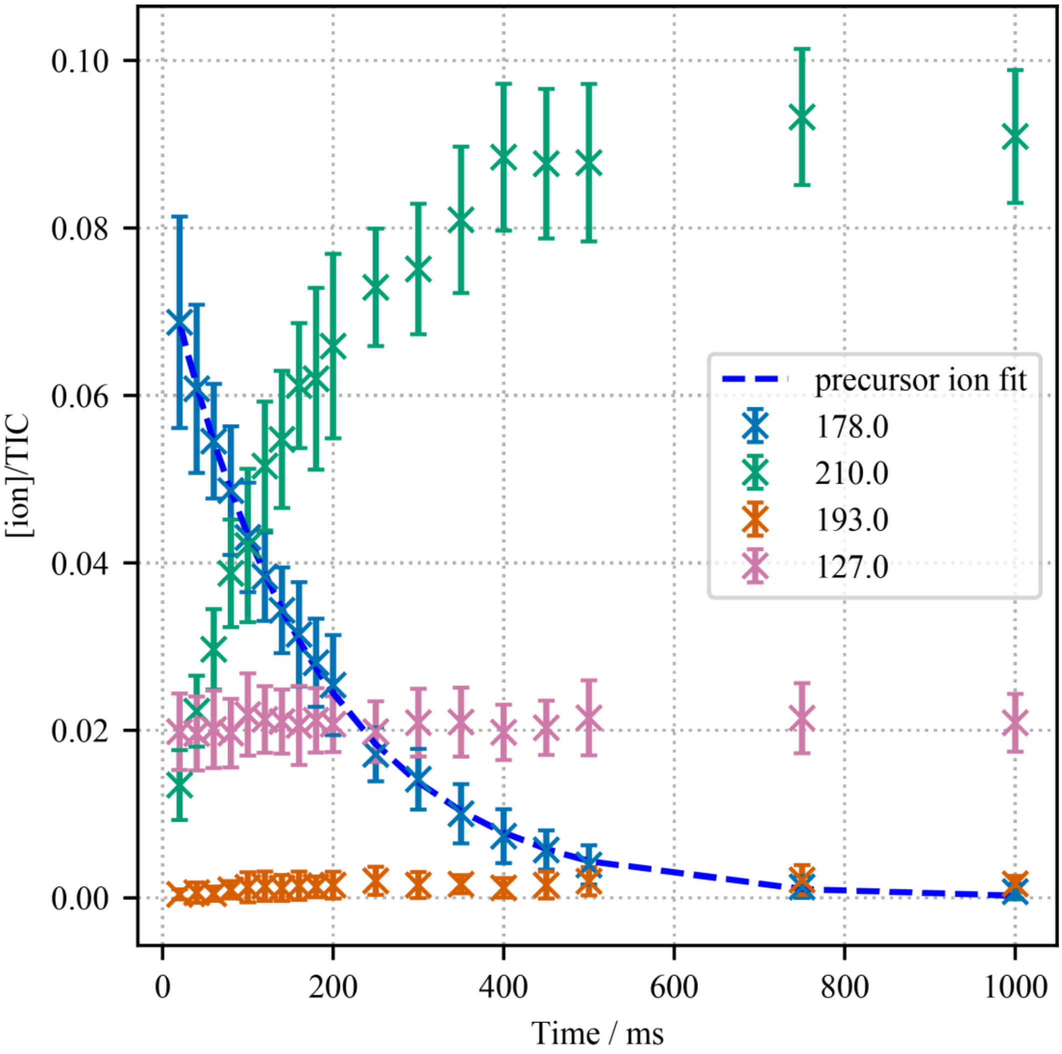

Figure S11. Kinetic profiles for the 3-dehydroadamantylcarboxylate anion (*m/z* 178) + O_2 reaction to give the dioxygen adduct (*m/z* 210) followed by loss of a hydroxyl radical (*m/z* 193). These data were acquired in an MS^2 experiment where radical anions were generated by photodissociation and allowed to react with oxygen in the linear ion trap without re-isolation, as depicted in Figure S7D. Decay of the reactant and evolution of product ions is normalised to the abundance of the unreactive iodide anion (*m/z* 127) formed in the photodissociation event to account for a loss of charge.

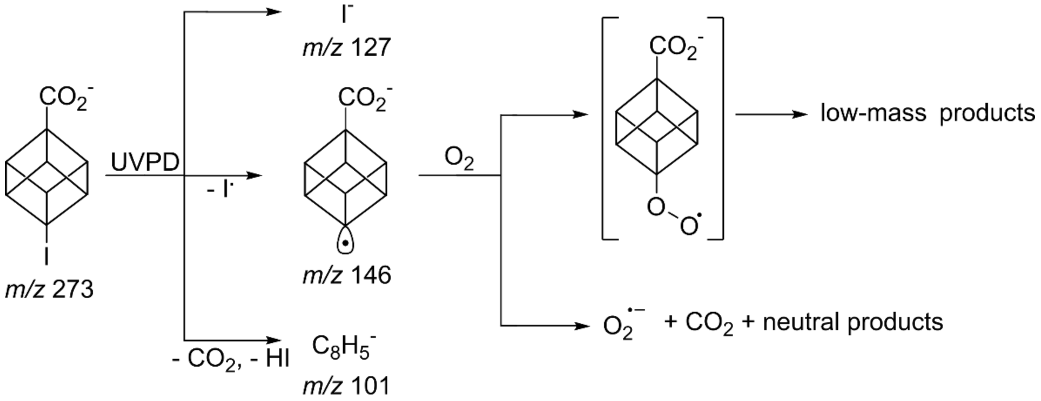

Scheme S1. Proposed reaction products following photodissociation of 4-iodocubylcarboxylate anion (*m/z* 273) and subsequent reaction of 4-dehydrocubylcarboxylate anion (*m/z* 146) with O_2. In addition to the iodide anion (*m/z* 127) generated upon photodissociation of the precursor ion (*m/z* 273), an ion proposed to be $C_8H_5^-$ (*m/z* 101) is also formed likely following decarboxylation (the abundance of this ion does not change with reaction time, see Figure S10). The loss of signal of the 4-dehydrocubylcarboxylate anion (*m/z* 146) with no observed increase in a product ion over time, together with the larger than predicted reaction efficiency (see Figure 2A), suggests that an alternative process is occurring and either (A) oxygen addition is occurring, but the peroxyl radical is unstable and fragments to undetectable low-mass products, or (B) oxygen addition is not competitive despite the submerged transition state. This alternative process is likely an electron transfer event occurring at the collision limit to give the dioxygen radical anion (*m/z* 32) and/or undetectable low-mass products (likely involving decarboxylation as suggested by the observation of *m/z* 101 upon photodissociation).

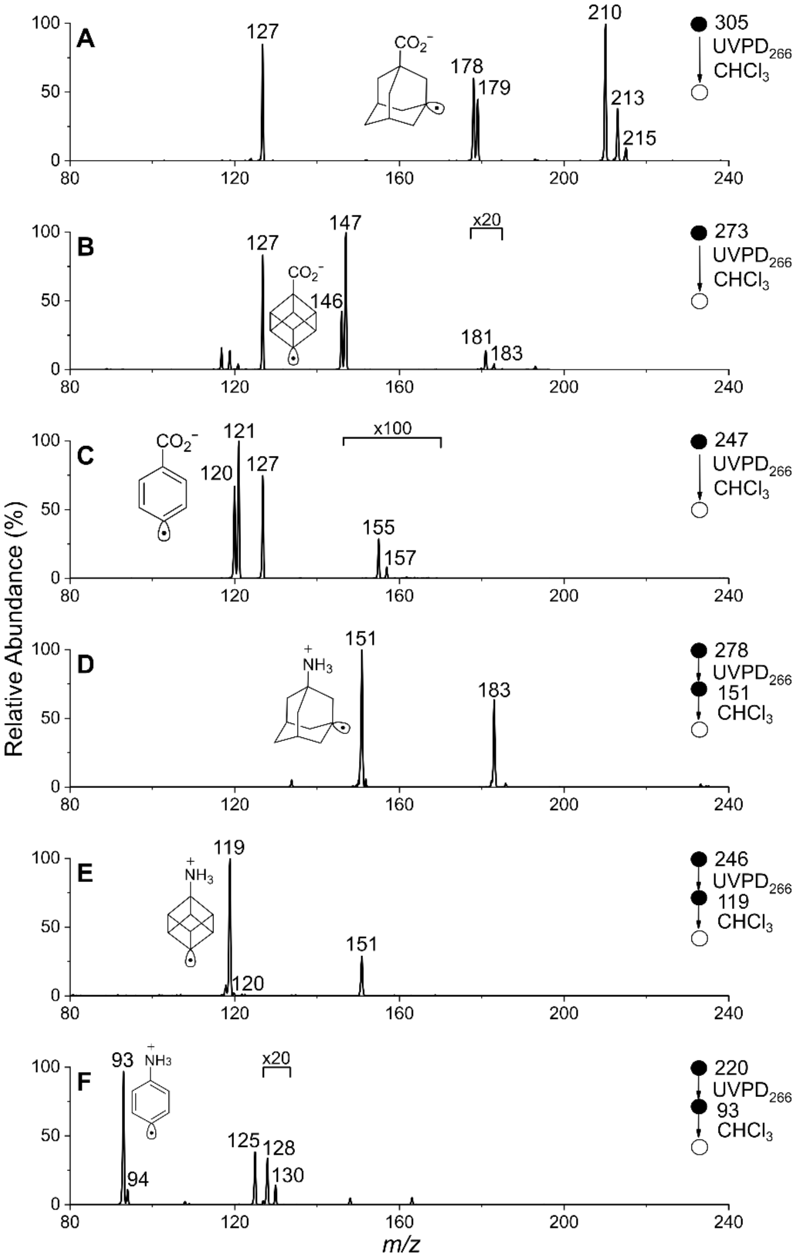

Figure S12. Representative mass spectra for distonic radical atom abstraction reactions with chloroform. **(A)** MS^2 mass spectrum of the carboxylatoadamantyl radical anion (*m/z* 178), the HAT product (*m/z* 179), and the CAT products (*m/z* 213 and *m/z* 215) after 1000 ms of reaction time; **(B)** MS^2 mass spectrum of the carboxylatocubyl radical anion (*m/z* 146), the HAT product (*m/z* 147), and the CAT products (*m/z* 181 and *m/z* 183) after 100 ms of reaction time (note that data was not recorded above *m/z* 200); **(C)** MS^2 mass spectrum of the carboxylatophenyl radical anion (*m/z* 120), the HAT product (*m/z* 121), and the CAT products (*m/z* 155 and *m/z* 157) after 100 ms of reaction time; **(D)** MS^3 mass spectrum of the ammoniumadamantyl radical cation (*m/z* 151) after 600 ms of reaction time; **(E)** MS^3 mass spectrum of the ammoniumcubyl radical cation (*m/z* 119) and the HAT product (*m/z* 120) after 6000 ms of reaction time; **(F)** MS^3 mass spectrum of the ammoniumphenyl radical cation (*m/z* 93), the HAT product (*m/z* 94), and the CAT products (*m/z* 128 and *m/z* 130) after 10,000 ms of reaction time. Iodide (*m/z* 127) is present in the radical anion MS^2 spectra from photodissociation of the iodine-containing precursor ion, whilst reactions with background O_2 are also observed in most cases.

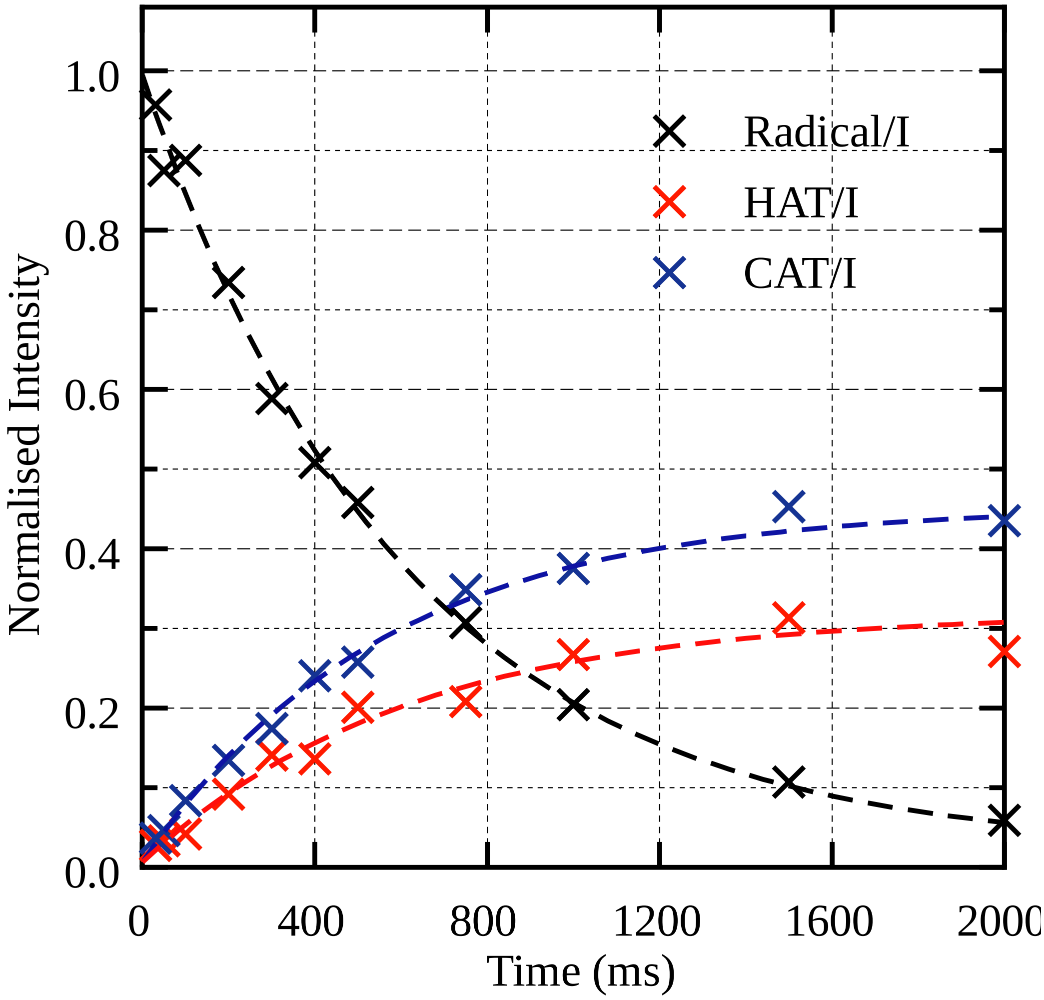

Figure S13. Kinetic profile for the reaction of the carboxylatoadamantyl radical anion (*m/z* 178) + chloroform reaction. These data were acquired in an MS^2 experiment where radical anions were generated by photodissociation and allowed to react with chloroform without re-isolation, as depicted in Figure S12A. Decay of the reactant and evolution of product ions is normalised to the abundance of the unreactive iodide anion (*m/z* 127) formed in the photodissociation event in order to account for competing reactions with background oxygen that result in a loss of charge.

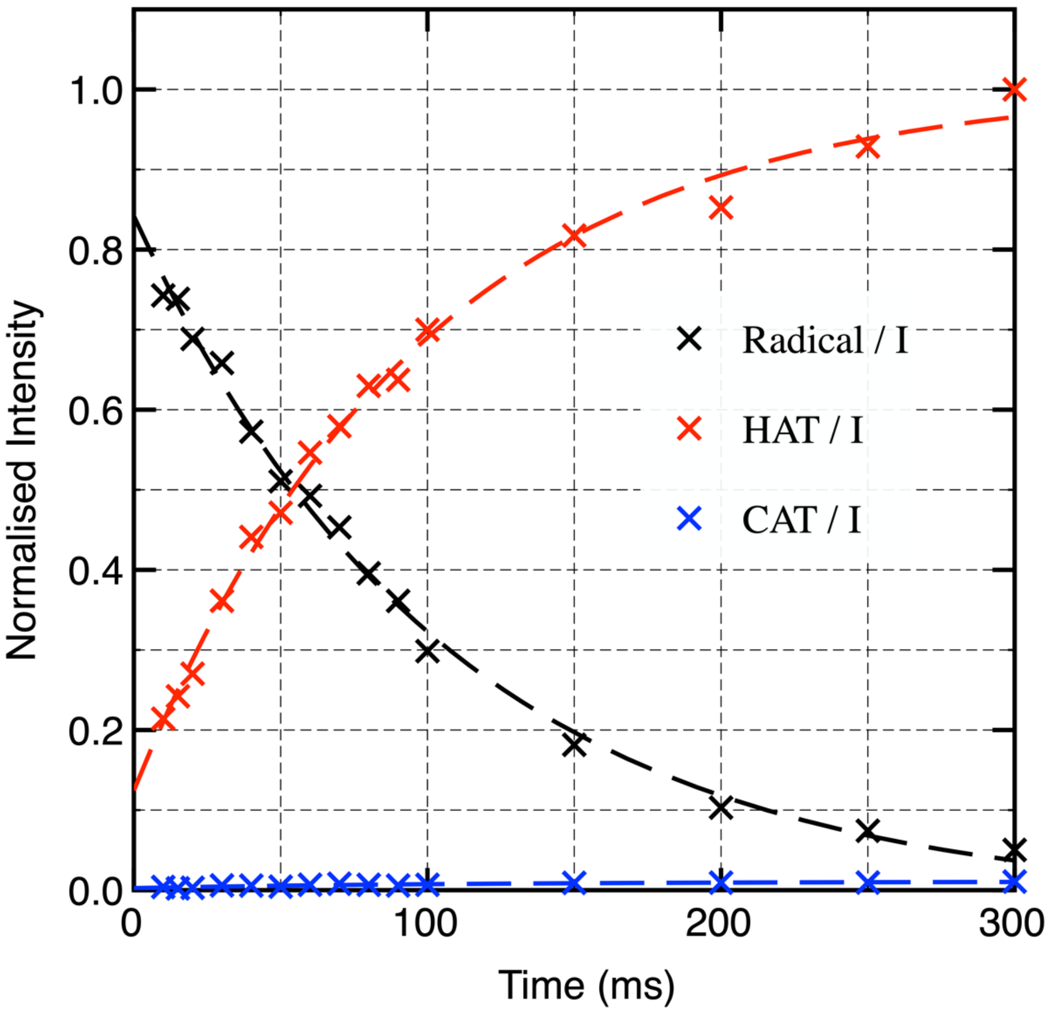

Figure S14. Kinetic profile for the reaction of the carboxylatocubyl radical anion (*m/z* 146) + chloroform reaction. These data were acquired in an MS^2 experiment where radical anions were generated by photodissociation and allowed to react with chloroform without re-isolation, as depicted in Figure S12B. Decay of the reactant and evolution of product ions is normalised to the abundance of the unreactive iodide anion (*m/z* 127) formed in the photodissociation event in order to account for competing reactions with background oxygen that result in a loss of charge.

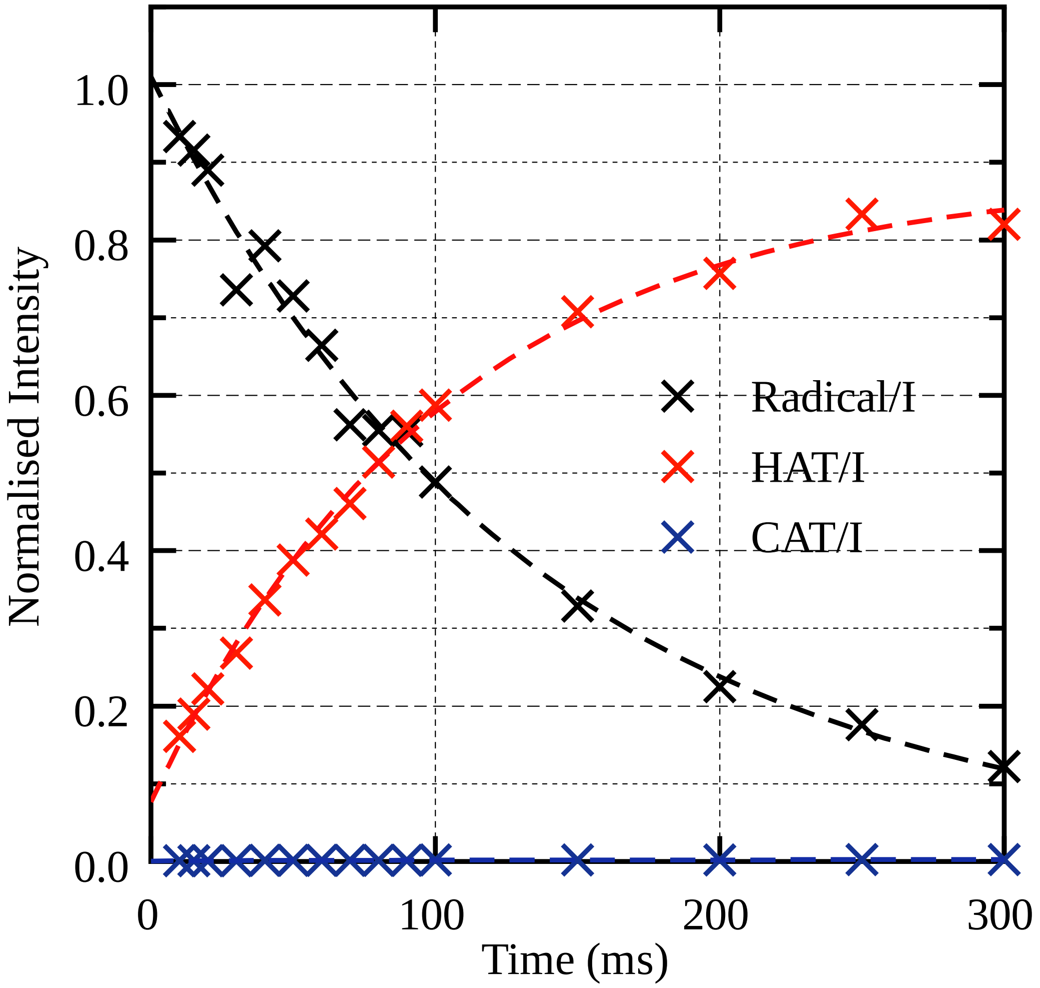

Figure S15. Kinetic profile for the reaction of the carboxylatophenyl radical anion (*m/z* 120) + chloroform reaction. These data were acquired in an MS^2 experiment where radical anions were generated by photodissociation and allowed to react with chloroform without re-isolation, as depicted in Figure S12C. Decay of the reactant and evolution of product ions is normalised to the abundance of the unreactive iodide anion (*m/z* 127) formed in the photodissociation event in order to account for competing reactions with background oxygen that result in a loss of charge.

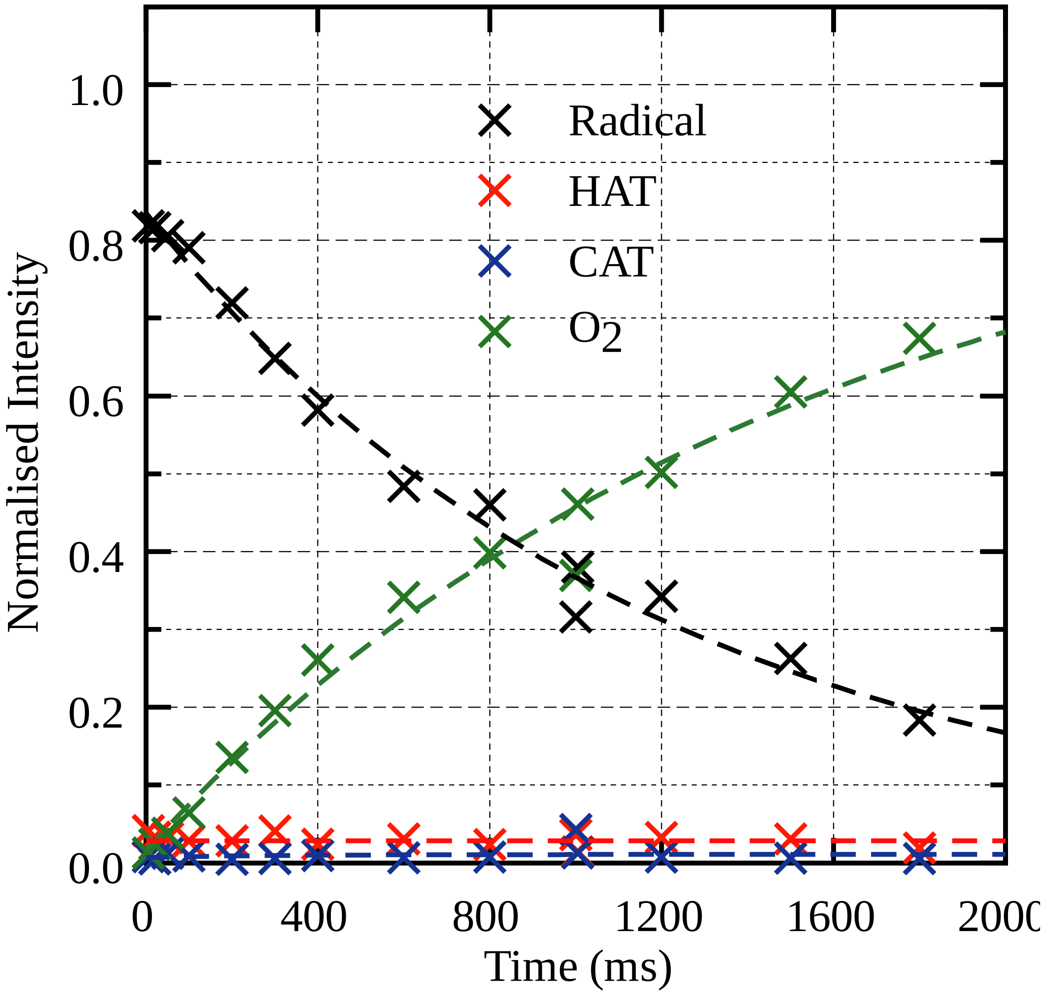

Figure S16. Kinetic profile for the reaction of the ammoniumadamantyl radical cation (*m/z* 151) + chloroform reaction. These data were acquired in an MS^3 experiment following mass-selection of the radical cation, as depicted in Figure S12D. Reactant and product signal intensities are each normalised to the total ion current in the MS^3 spectra.

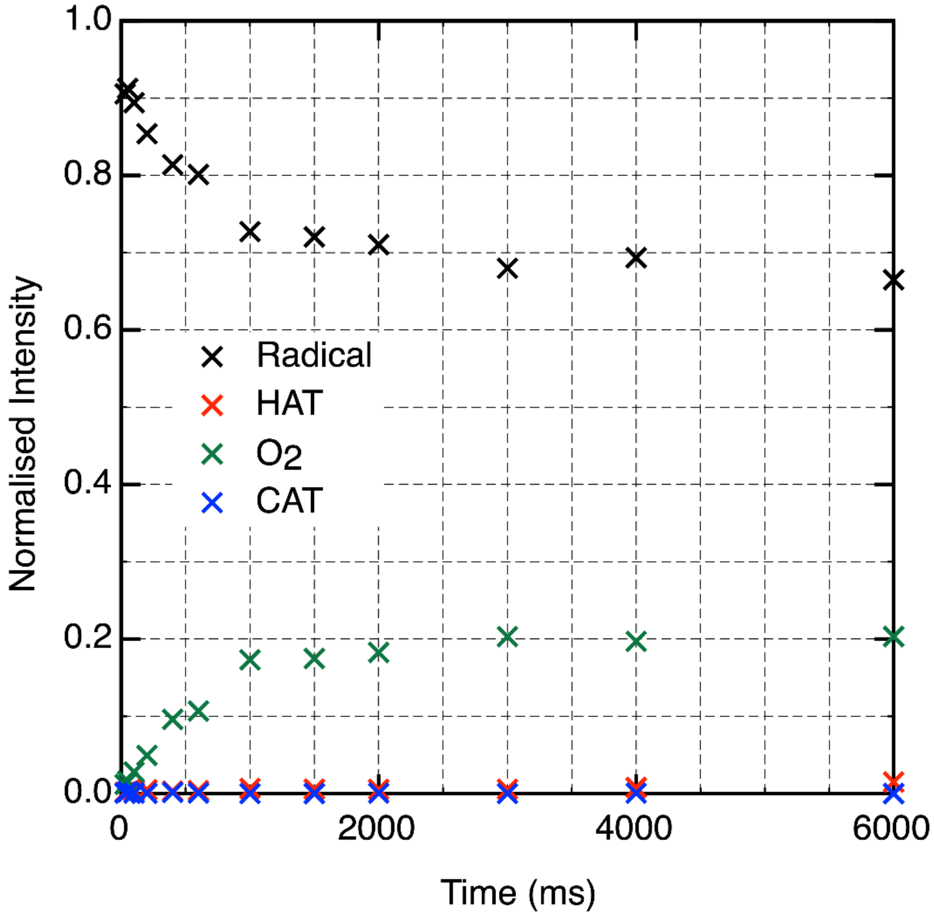

Figure S17. Kinetic profile for the reaction of the ammoniumcubyl radical cation (*m/z* 119) + chloroform reaction. These data were acquired in an MS^3 experiment following mass-selection of the radical cation, as depicted in Figure S12E. Reactant and product signal intensities are each normalised to the total ion current in the MS^3 spectra.

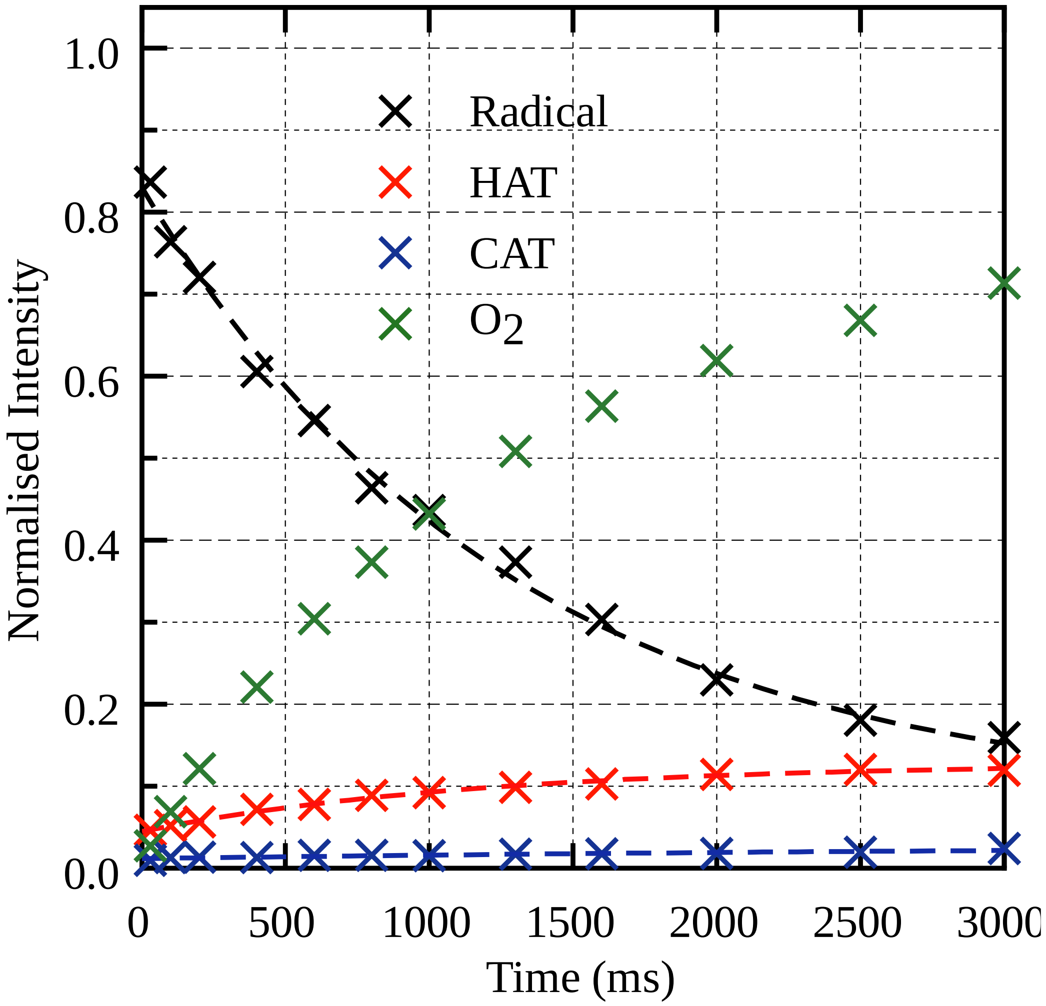

Figure S18. Kinetic profile for the reaction of the ammoniumphenyl radical cation (*m/z* 93) + chloroform reaction These data were acquired in an MS^3 experiment following mass-selection of the radical cation, as depicted in Figure S12F. Reactant and product signal intensities are each normalised to the total ion current in the MS^3 spectra.

Experimental Set-up

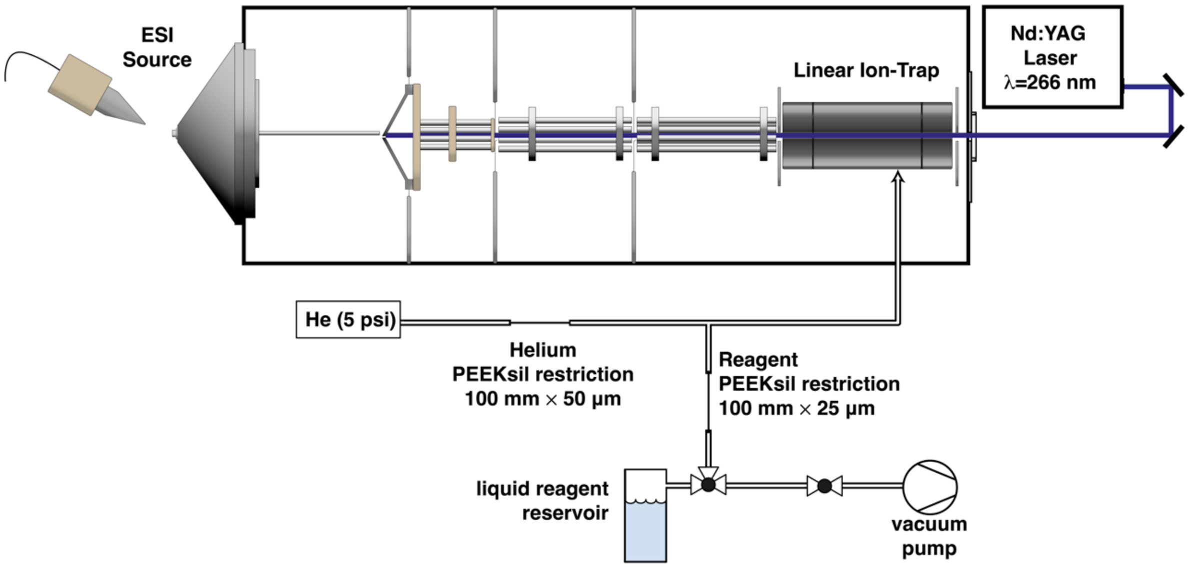

Scheme S2. Custom-built gas mixing manifold for introduction of chloroform seeded in the helium buffer gas into the linear ion-trap.[1]

Table S1. Relative *pseudo* first-order (k_1) reaction rate constants for dioxygen reaction with the adamantyl (reaction **10**) and phenyl (reaction **11**) distonic radical anions across different helium gas pressure regimes compared to the relative second-order (k_2) reaction rate constants in Table 1.

Instrument	Trap pressure (mTorr)	k_2 (**10**) /k_2 (**11**)
LTQ XL	2.5	1.6 ± 0.2
		k_1 (**10**) /k_1 (**11**)
LTQ Velos HP trap	5	1.8 ± 0.2
LTQ Velos LP trap	<1	1.8 ± 0.2

Table S2. Optimised transition state energies for neutral radical reactions in this study calculated at DSD-PBEP86-D3(BJ)/aug-cc-pVTZ.

Radical	**TS (kJ mol^{-1})**
phenyl	-0.61
4-fluorophenyl	-1.5
4-methylphenyl	-0.41
4-hydroxyphenyl	-1.5
4-cyanophenyl	-0.50
4-benzylphenyl	-0.22

Dipole Moments for Chloroform Reactions

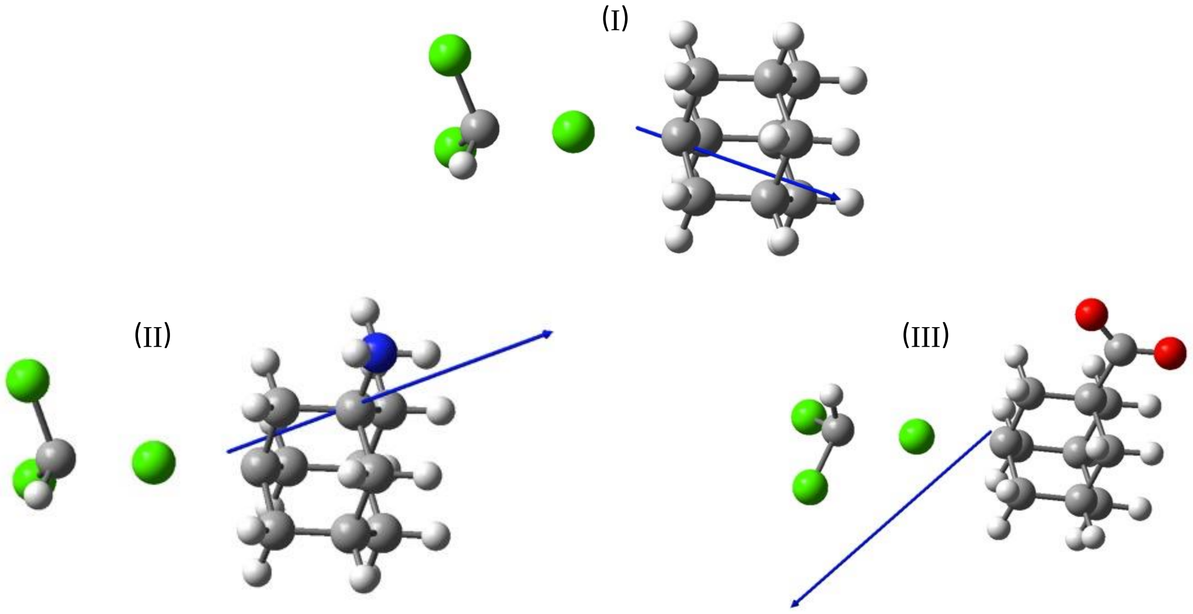

Figure S19. Optimised structures and dipole moments for the CAT reaction between chloroform and (i) adamantyl, (ii) ammoniumadamantyl, and (ii) carboxylatoadamantyl. For the two charged functional systems the dipole moment is scaled by 0.5.

In Figure S19 the neutral system shows the orientation of the TS dipole moment without a charged function group which points towards the bottom of the molecule (in this orientation). For the ammoniumadamantyl radical reaction the orientation of the chloroform remains the same to minimise the destabilisation effect of the unfavourable positively charged OEF (as the dipole moment will point more off axis). In contrast, for the carboxylatoadamantyl radical reaction the orientation of the chloroform has flipped which will align the dipole more towards favourable negatively charged OEF and maximise the stabilisation effect induced by this interaction.

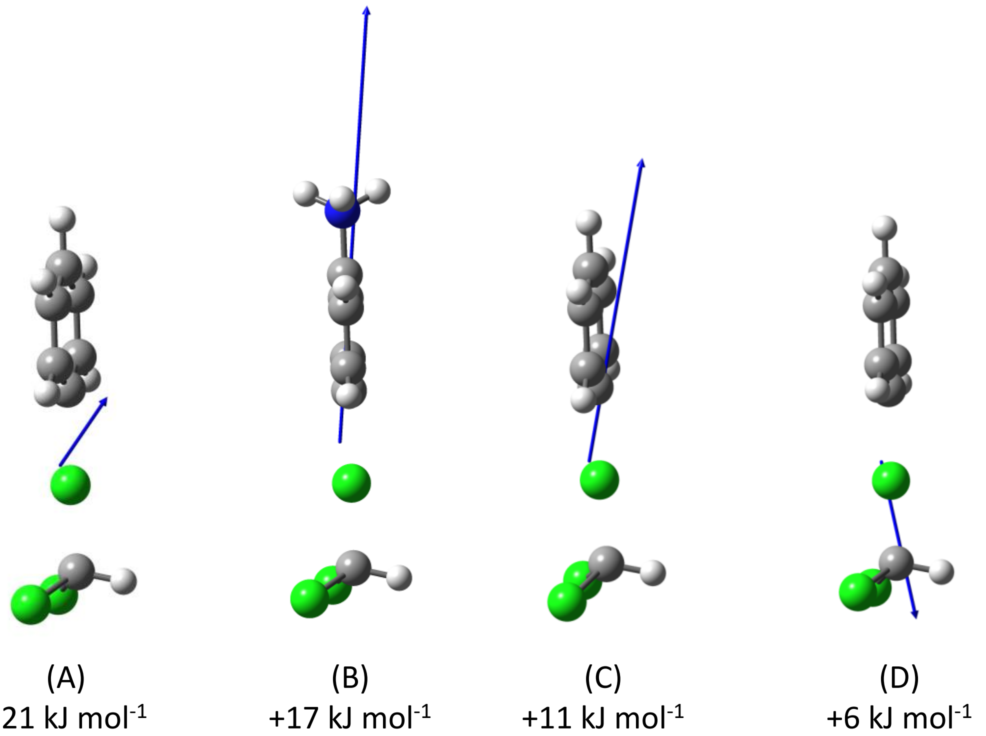

Figure S20. (A) Geometry and energy of CAT for phenyl. (B) Geometry and energy of CAT for phenyl-NH_3^+ at the DSD-PBEP86-D3(BJ)/aug-cc-pVTZ level of theory. Geometry and energy of CAT for phenyl with a (C) negative and (D) positive point charge.

The major difference between the cubyl and phenyl radicals in Figure S19 is the structure of the 3D electron density cloud, caused by the number of atoms around the radical molecule. In the HAT TS, the dipole points directly and symmetrically towards the end of the molecule so there is no significant difference between phenyl and cubyl radicals. However, with CAT the dipole points off axis asymmetrically due to the orientation of the R–Cl–CCl_2H moiety. For the phenyl radical the Cl-C-H bond angle decreases from the ideal tetrahedral angle of 109.5, tilting the dichloromethyl group and shifting the dipole closer to the end of the molecule to compensate for this off axis effect. In all cases for CAT the phenyl TS has a lower Cl-C-H bond angle compared to the corresponding cubyl TS (see figure above). This increases the strain at the TS, raising the calculated barrier. For the cubyl radical, this off axis effect is suppressed due to the increased electron density at the end of the molecule so the TS is less strained (larger Cl-C-H bond angle) which will reduce the barrier compared to the phenyl radical. In contrast, substitution with a cationic charged functional group flips the order of stability since it is more favourable for the dipole to point away from a destabilising field. This manifests as a decrease in the Cl-C-H bond angle, compared to the neutral and anionic systems for the CAT reactions.

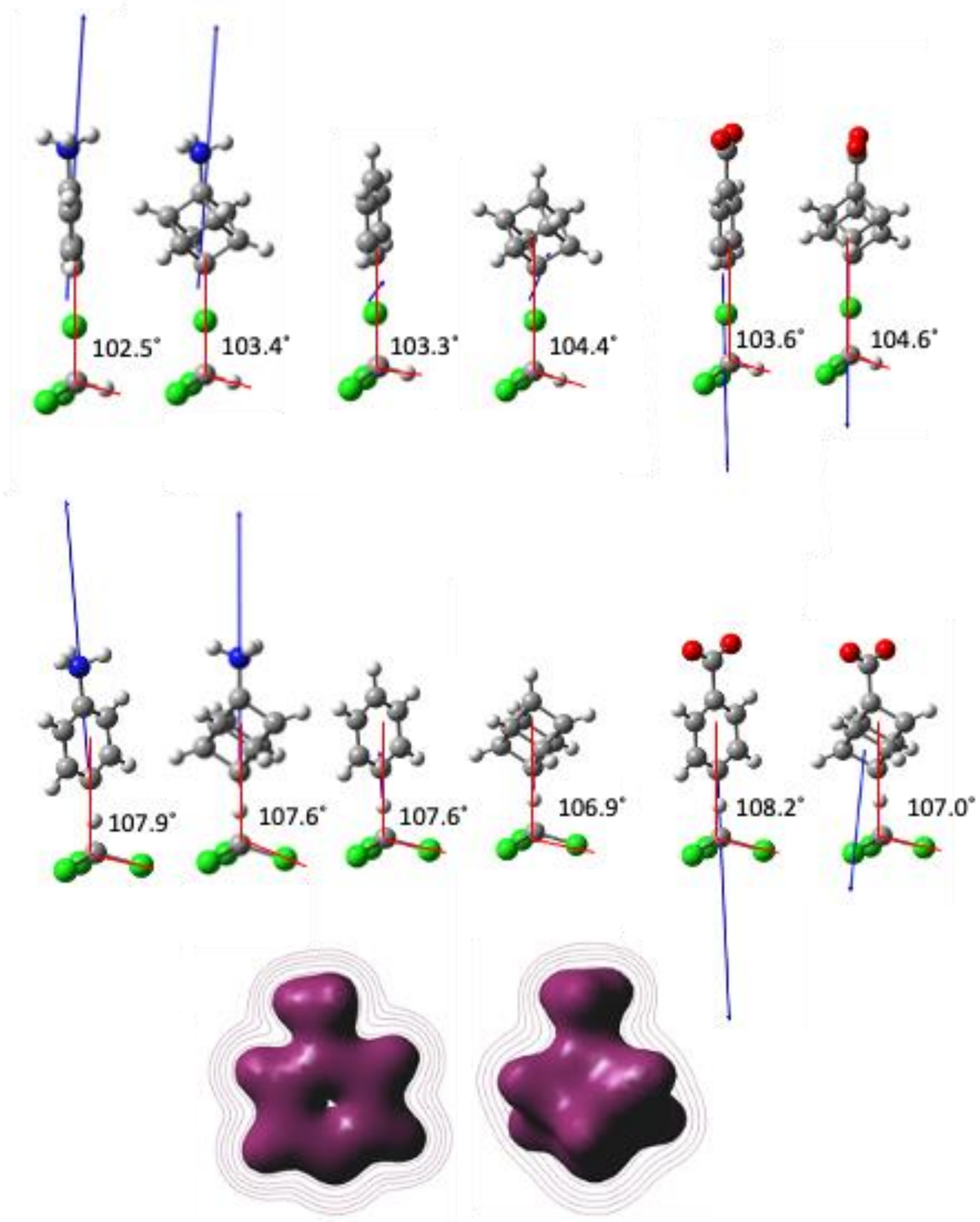

Figure S21. Optimised structures, dipole moments (scaled by 0.5), and key bond angles of the HAT and CAT TSs of the cationic, neutral, and anionic cases of the phenyl and cubyl reactions. These structures rationalise the asymmetric (de)stabilisation of the CAT barriers between these two radicals. The density of the 3D electron cloud for the phenyl-NH_3^+ and the cubyl-NH_3^+ radicals are included below. In these images the isoval of the surface is 0.03, while the isoval of the contours are 8.

Table S3. Comparison between DSD-PBEP86-D3(BJ) calculations using the aug-cc-pVTZ (TZ) and the aug-cc-pVDZ (DZ) level of theory.

Radical	**TZ TS Energy (kJ mol^{-1})**	**DZ TS Energy (kJ mol^{-1})**	**Absolute Difference**
4-dehydrocubylammonium cation	+5.8	+6.1	0.3
4-dehydroanilinium cation	+1.4	+2.6	1.2
2-methyl-4-dehydroanilinium cation	–0.1	-1.7	1.6
2-hydroxy-4-dehydroanilinium cation	+1.2	+0.6	0.6
4-dehydrocarboxylatophenyl anion	–6.7	-4.4	2.3
4-dehydrosulfonatophenyl anion	–5.6	-7.0	1.4
		Average	1.2

Table S4. Experimental *pseudo* first-order (k_1) and second-order (k_2) rate constants and reaction efficiencies (Φ) for HAT and CAT for the four distonic radical ion reactions with chloroform.

Radical	**HAT**			**CAT**		
	k_1 (s^{-1})	k_2 *	Φ (%)	k_1 (s^{-1})	k_2 *	Φ (%)
			Cationic			
Adamantyl-NH_3^+	NR$_{obs}$	< 1 × 10^{-15}	< 0.0001	NR$_{obs}$	< 1 × 10^{-15}	< 0.0001
Cubyl-NH_3^+	0.002 ± 0.005	0.3 ± 0.6 × 10^{-14}	0.0003	NR$_{obs}$	< 1 × 10^{-15}	< 0.0001
Phenyl-NH_3^+	0.01 ± 0.001	4.7±0.5 × 10^{-14}	0.004	0.001 ± 0.0005	0.7±0.2 × 10^{-14}	0.0006
			Anionic			
Adamantyl-CO_2^-	1.10 ± 0.12	4.1 ± 0.6 × 10$^{-13\,\#}$	0.04	1.23 ± 0.11	6.5 ± 1 × 10$^{-13\,\#}$	0.07
Cubyl-CO_2^-	19.4 ± 0.22	8.8 ± 0.1 × 10^{-12}	0.91	0.12 ± 0.05	5.4 ± 2.1 × 10^{-14}	0.006
Phenyl-CO_2^-	9.8 ± 0.5	8.7±0.3 × 10^{-12}	0.86	1.2 ± 0.8	1.9±0.5 × 10^{-14}	0.002

*units of k_2 are cm^3 molecule^{-1} s^{-1}. $^{\#}k_2$ values were taken from Harman and Blanksby[2] and used to determine the number density of $CHCl_3$ in this study, which varied across days for measurements and so the adamantyl-CO_2^- reaction was repeated for consistency. Note that the k_1 values for product ion growth determined by a single exponential fit are not strictly *pseudo* first-order in all cases (as the corresponding logarithmic plot is not linear for the entire reaction time range), and so are less reliable than the branching ratios reported in Table 2, which are the ratios of the asymptotes of each product channel. Furthermore, the kinetics for the cationic species with chloroform are close to or at the limit of detection for the current experimental set-up[3] and in some cases no reaction is observed (NR_{obs}).

Table S5. Natural spin densities of the three atoms involved in the key transition state for HAT and CAT of the neutral cubyl radical reaction with chloroform.* The majority of the spin density is located on the carbon centred radicals in this neutral system, suggesting that the contribution of the ionic resonance structure is near zero and will only play a significant role in the presence of an electrostatic field.

	C (Cubyl)	**C ($CHCl_3$)**	**X**
HAT (X = H)	0.553	0.410	-0.085
CAT (X = Cl)	0.574	0.430	-0.109
Estimated weighting of resonance structures	~ 60%	~ 40%	~ 0%

*calculated at DSDPBEP86/aug-cc-pVDZ from natural population analysis using NBO program version 7.0.10 developed by Glending and co-workers.[4]

Abbreviations

°C	degrees Celsius
Δ	heat/reflux
δ	chemical shift
$h\upsilon$	photoirradiation
^{1}H	proton isotope
^{13}C	carbon isotope
ca	circa (approximately)
calcd	calculated
$CDCl_3$	deuterated chloroform
$CHCl_3$	chloroform
dec	decomposed
DCM	dichloromethane
DMF	*N*,*N*-dimethylformamide
DMDS	dimethyldisulfide
DPPA	diphenylphosphoryl azide
EI	electron ionisation
ESI	electrospray ionisation
et al	et alii / et aliae (and others)
eq	equivalents
g	gram
HCl	hydrochloric acid
h	hour(s)
HRMS	high resolution mass spectrometry
Hz	Hertz
in vacuo	in a vacuum
in vivo	within the living
IR	infrared
J	coupling constant
L	litre
M	molar
MeOH	methanol
mg	milligrams
MHz	mega-Hertz
min	minute(s)
mL	millilitre(s)
mmol	millimole(s)
mol	moles
m.p	melting point
m/z	mass to charge ratio
NaOH	sodium hydroxide
NMR	nuclear magnetic resonance
ppm	parts per million
RBF	round bottom flask
R_f	retention factor

RT	retention time	TLC	thin layer chromatography
rt	room temperature	v/v	volume per volume
t	tertiary	w/w	weight per weight
t-BuOH	tertiary butanol	µL	microlitre
TEA	triethylamine	UV	ultraviolet
THF	tetrahydrofuran		

General Remarks

NMR spectra were recorded under standard conditions (unless stated otherwise) using Bruker AV 500, 400 and 300 MHz or Bruker AS 500 MHz spectrometers and were referenced with residual monoprotic solvent peaks (e.g. $CDCl_3$, C_6D_6 etc.) [5]. Coupling constants (*J*) are quoted to the nearest 0.1 Hz. The following abbreviations are used to report multiplicities: s = singlet, d = doublet, t = triplet, m = multiplet, quin = quintet, sext = sextet, sep = septet, br. = broad. High resolution ESI mass spectra were recorded using a Bruker MicroTOF-Q (quadrupole-Time of Flight) with a Bruker ESI source. High resolution EI mass spectra were acquired on a Thermo Scientific Q Exactive GC equipped with a TriPlus RSH autosampler, SSL injector and Thermo TG5SilMS 30 m x 0.25 mm x 0.25 µm analytical column. Melting points were determined using a Digimelt MPA 160 melting point apparatus and are reported uncorrected. Flash column chromatography was run using Merck silica gel 60 (230–400 mesh). Fractions were initially visualised using UV irradiation and subsequently by heating TLC plates exposed to either ceric ammonium molybdate (Goofy's stain) or 10 % aqueous potassium permanganate. TLC was performed with Merck precoated silica gel plates (silica gel 60 F_{254}) 0.2 mm). Argon was dried by passing through a drying tube containing 4Å molecular sieves and Drierite™. Glassware was oven dried (160 °C) before use with anhydrous solvents and reagents. THF was freshly distilled to dryness over elemental sodium/benzophenone under an argon atmosphere. DCM was freshly distilled to dryness over calcium hydride under an argon atmosphere. Unless stated otherwise commercially available chemicals were used without further purification. 2-Mercaptopyridine *N*-oxide sodium salt (PSS) was concentrated to dryness then washed with ethyl acetate. Diphenylphosphoryl azide (DPPA) was distilled to dryness following known procedures.[6] *t*-Butanol, *N*,*N*-dimethylformamide (DMF), triethylamine (TEA), and *N*,*N*-diisopropylamine were freshly distilled to dryness over calcium hydride under an argon atmosphere or reduced pressure.[7]

Synthetic Procedures and Characterisation Data

4-(Methoxycarbonyl)cubane-1-carboxylic acid (**S2**)

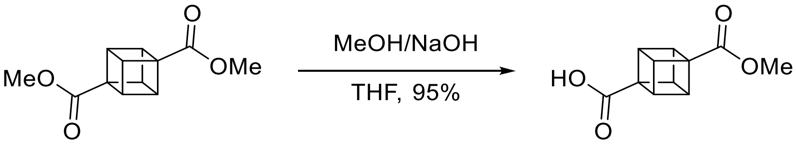

S1 **S2**

Following the procedure of Eaton *et al.*:[8] dimethyl cubane-1,4-dicarboxylate (**S1**) (6.079 g, 27.60 mmol) was dissolved in THF (250 mL). A solution of sodium hydroxide (1.220 g, 30.50 mmol) in methanol (14 mL) was added dropwise and the solution was left to stir for 16 h. The THF was removed *in vacuo* and the residual solid was dissolved in water (200 mL) then washed with DCM (3 x 100 mL).

The aqueous phase was acidified to pH 2 with hydrochloric acid (10 M) then extracted with DCM (3 x 100 mL). The combined organic phases were dried over magnesium sulfate and concentrated to give the title compound **S2** (5.385 g, 95%) as a white solid. ^{1}H-NMR (300 MHz, CDCl$_3$): δ (ppm) 4.28 (m, 6H), 3.73 (s, 3H).

Methyl 4-iodocubane-1-carboxylate (**S3**)

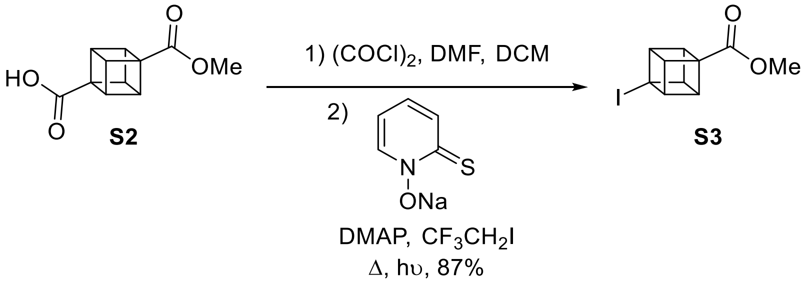

Following the procedure of Priefer *et al*:[9] to a solution of 4-methoxycarbonylcubane-1-carboxylic acid (**S2**) (1.000 g, 4.84 mmol) in anhydrous DCM (50 mL) was added oxalyl chloride (0.50 mL, 5.82 mmol) and anhydrous DMF (1 drop) under an argon atmosphere. After 1 h, the mixture was concentrated *in vacuo* and further dried under high vacuum (1 h). Separately, freshly ground 2-mercaptopyridine *N*-oxide sodium salt (952 mg, 6.38 mmol), DMAP (6 mg, 0.049 mmol) and 2,2,2-trifluoroiodoethane (2.39 mL, 24.20 mmol) were dissolved in anhydrous DCM (50 mL) and heated to reflux under an argon atmosphere whilst under irradiation from a 500-W tungsten lamp. The newly formed acid chloride was dissolved in anhydrous DCM (50 mL) and added slowly to the refluxing mixture. After reflux (3 h) the suspension was washed with water (3 x 50 mL) then dried over magnesium sulfate. Concentration and purification by column chromatography (50% ethyl acetate/petroleum ether v/v) gave the title compound **S3** (1.210 g, 87%) as an off-yellow solid. ^{1}H-NMR (300 MHz, CDCl$_3$): δ (ppm) 4.40–4.36 (m, 3H), 4.30–4.26 (m, 3H), 3.70 (s, 3H).

4-Iodocubane-1-carboxylic acid (**S4**)

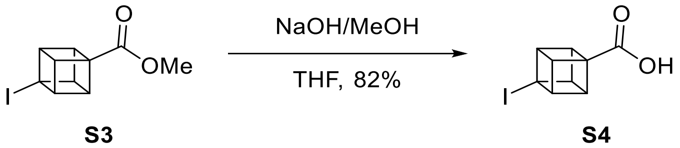

Adapted from the procedure of Priefer *et al*:[9] methyl 4-iodocubane-1-carboxylate (**S3**) (5.449 g, 18.91 mmol) was dissolved in THF (200 mL). A solution of sodium hydroxide (1.037 g, 25.93 mmol) in methanol (6 mL) was added dropwise and the solution was left to stir for 16 h. The THF was removed *in vacuo* and the residual solid was dissolved in water (200 mL) and washed with DCM (3 x 100 mL). The aqueous phase was acidified to pH 2 giving the title compound **S4** (4.264 g, 82%) as a white solid which was collected by filtration. ^{1}H-NMR (300 MHz, MeOD): *δ* (ppm) 4.38–4.33 (m, 3H), 4.27–4.21 (m, 3H).

4-Iodocubane-1-*t*-butyl carbamate (**S5**)

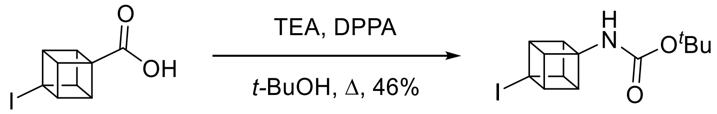

S4 **S5**

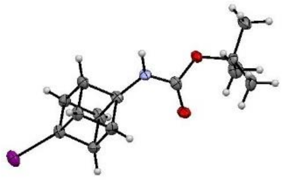

S5

X-ray

Adapted from the procedure of Shiori *et al*:[10] 4-iodocubane-1-carboxylic acid (**S4**) (200 mg, 0.73 mmol)), anhydrous diphenylphosphoryl azide (0.19 mL, 0.88 mmol) and anhydrous triethylamine (0.12 mL, 0.88 mmol) were dissolved in anhydrous *t*-butanol (4 mL) under an argon atmosphere. The mixture was left to stir at rt for 30 min, at reflux for 2 h, then room temperature for 16 h. The resulting precipitate was collected by filtration and washed with ice cold isopropanol to give the title compound **S5** (116 mg, 46%) as white crystals [Note: the presence of amide rotamers made the acquisition of a satisfactory ^{13}C spectrum problematic.] m.p. 166 °C (dec); ^{1}H-NMR (500 MHz, MeOD): δ (ppm) 4.20–4.05 (m, 6H), 1.44 (s, 9H); HRMS-EI calcd for $C_{13}H_{16}NO_2I$ ($[M]^{\bullet +}$): 345.0220; found: 345.0218.

4-Iodocubane-1-amino hydrochloride (**S6**)

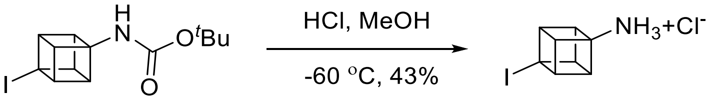

S5 **S6**

Adapted from the procedure of Eaton *et al*:[11] 4-Iodocubane-1-*t*-butyl carbamate (**S5**) (52 mg, 0.15 mmol) was dissolved in anhydrous methanol (3 mL) under an argon atmosphere and cooled to -60 °C. HCl gas was bubbled through the mixture for 1 min before warming to rt. After stirring for 4 h, the methanol was removed *in vacuo* and the resulting precipitate was collected by recrystallisation (20% acetone/diethyl ether v/v) to give the title compound **S6** (18 mg, 43%) as a pale yellow solid. m.p. 162 °C (dec); ^{1}H-NMR (500 MHz, MeOD): δ (ppm) 4.35–4.33 (m, 3H), 4.22–4.20 (m, 3H); ^{13}C-NMR (125 MHz, MeOD): δ (ppm) 66.7, 53.4, 52.0, 35.9; HRMS-ESI calcd for C_8H_9NI ($[M-Cl]^+$): 245.9774; found: 245.9780.

^{1}H and ^{13}C Spectra

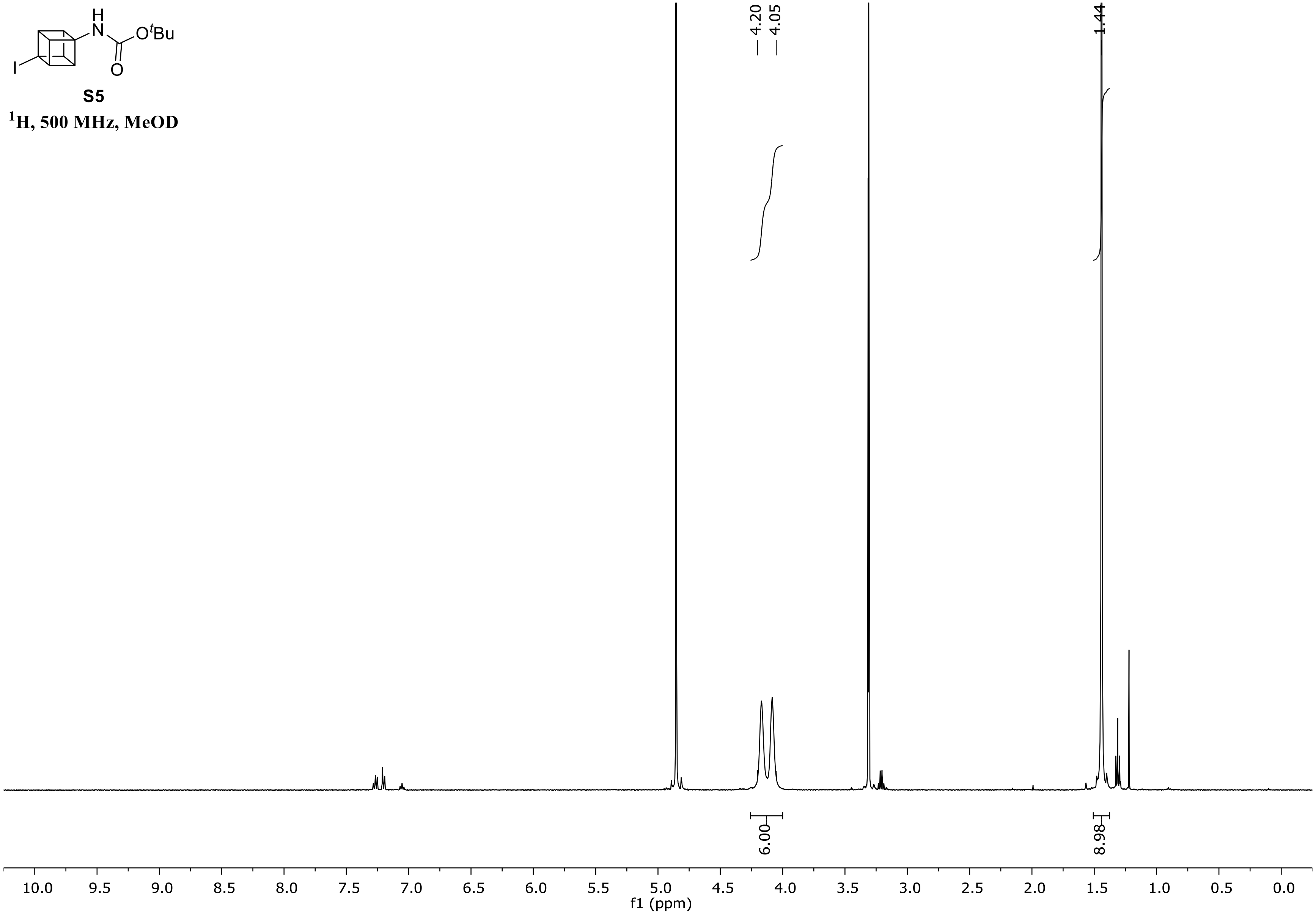

S5

^{1}H, 500 MHz, MeOD

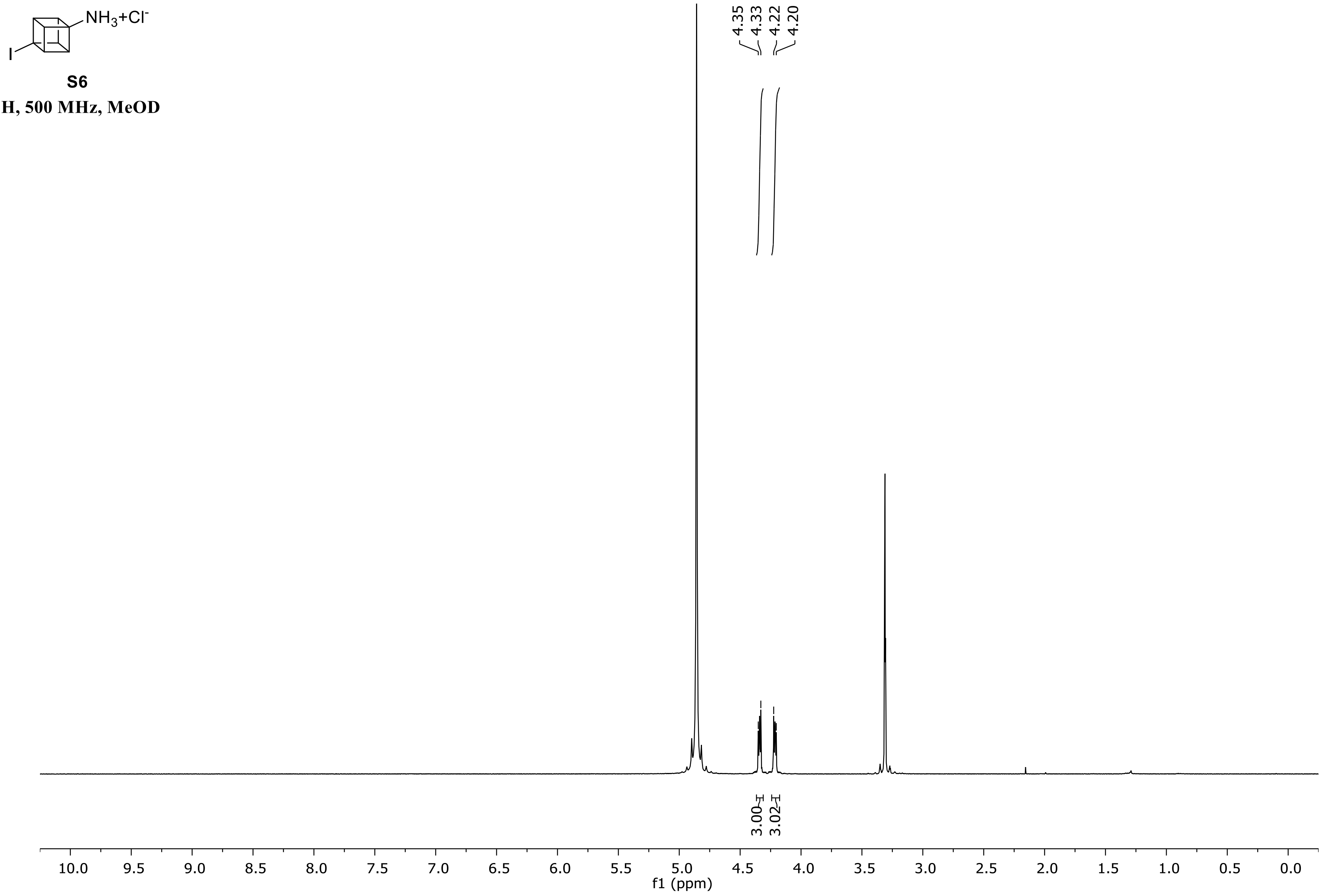

S6

^{1}H, 500 MHz, MeOD

S6

^{13}C, 125 MHz, MeOD

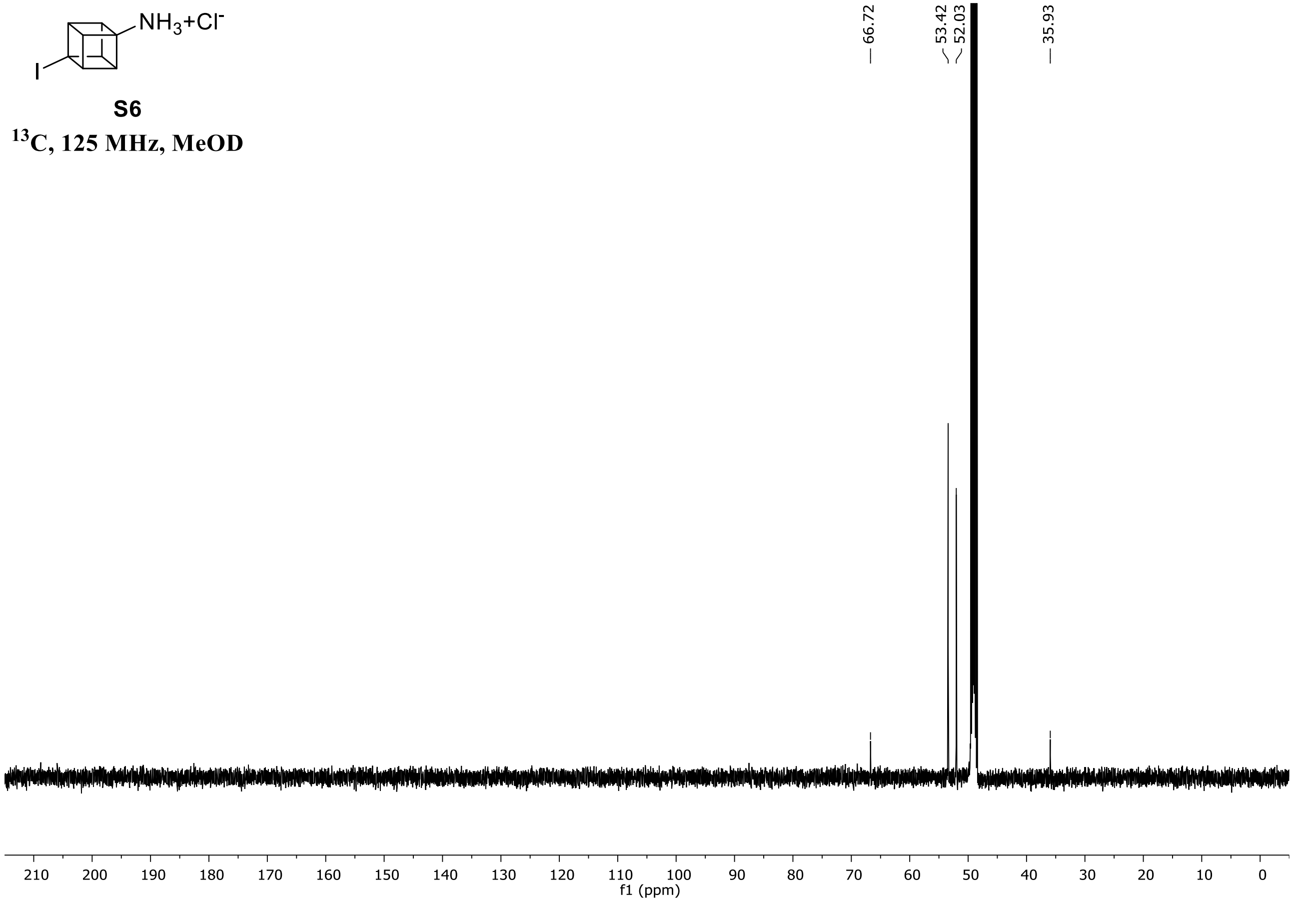

Crystallographic Data

4-Iodocubane-1-*t*-butyl carbamate (**S6**)

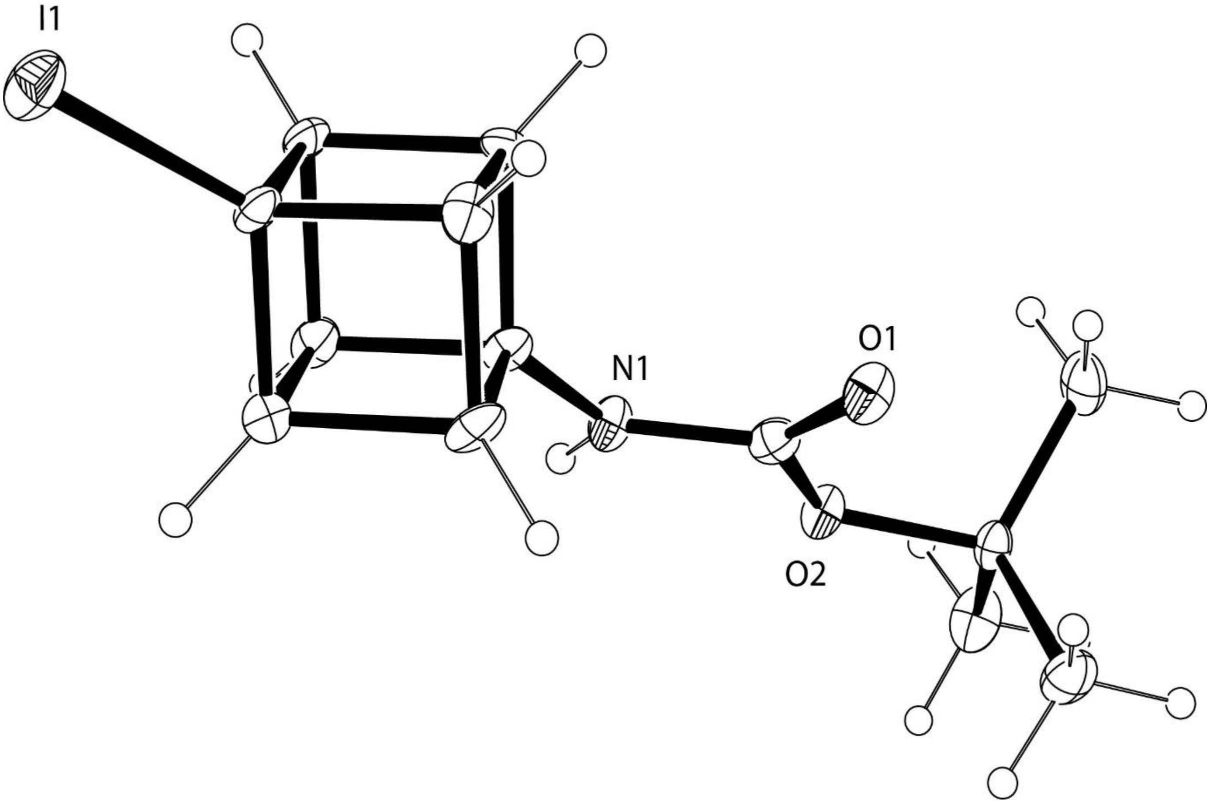

Identification code	1820sdh-viii-099	
Empirical formula	C_{13} H_{16} I N O_2	
Formula weight	345.17	
Temperature	190(2) K	
Wavelength	0.71073 Å	
Crystal system	Triclinic	
Space group	$P\ \bar{1}$	
Unit cell dimensions	a = 5.4287(7) Å	α= 96.706(11)°.
	b = 8.9764(12) Å	β= 95.087(10)°.
	c = 13.4695(16) Å	γ = 90.122(11)°.
Volume	649.26(14) $Å^3$	
Z	2	
Density (calculated)	1.766 Mg/m^3	
Absorption coefficient	2.456 mm^{-1}	
F(000)	340	

Crystal size	0.386 x 0.126 x 0.041 mm^3
Theta range for data collection	3.60 to 25.00°.
Index ranges	-6<=h<=6, -10<=k<=9, -15<=l<=15
Reflections collected	4332
Independent reflections	2289 [R(int) = 0.0477]
Completeness to theta = 25.00°	99.8 %
Absorption correction	Analytical
Max. and min. transmission	0.906 and 0.625
Refinement method	Full-matrix least-squares on F^2
Data / restraints / parameters	2289 / 0 / 154
Goodness-of-fit on F^2	1.173
Final R indices [I>2sigma(I)]	R1 = 0.0646, wR2 = 0.1368
R indices (all data)	R1 = 0.0775, wR2 = 0.1444
Largest diff. peak and hole	1.734 and -1.358 e.Å^{-3}

Crystallographic data were collected on an Oxford Diffraction Gemini CCD X-ray diffractometer using Mo-Kα (0.710713 Å) radiation. The sample was cooled to 190 K with an Oxford Cryosystems Desktop Cooler. The structure was solved with SHELXS and refined with SHELXL[12] and all calculation were carried out within the WinGX package.[13] Analytical absorption corrections were applied within the CrysAlisPro program although residual extrema in the vicinity of the iodine atom remained at the end of refinement. The thermal ellipsoid diagram was generated with ORTEP3.[14] Crystallographic data in CIF format have been deposited with the Cambridge Crystallographic Data Centre (CCDC 2336194).

Bibliography

1. Williams, P. E.; Marshall, D. L.; Poad, B. L.; Narreddula, V. R.; Kirk, B. B.; Trevitt, A. J.; Blanksby, S. J., Comparing positively and negatively charged distonic radical ions in phenylperoxyl forming reactions. *J. Am. Soc. Mass. Spectrom.* **2018,** *29* (9), 1848-1860.
2. Harman, D. G.; Blanksby, S. J., Investigation of the gas phase reactivity of the 1-adamantyl radical using a distonic radical anion approach. *Org. Biomol. Chem.* **2007,** *5* (21), 3495-3503.
3. Bhujel, M.; Marshall, D. L.; Maccarone, A. T.; McKinnon, B. I.; Trevitt, A. J.; da Silva, G.; Blanksby, S. J.; Poad, B. L. J., Gas phase reactions of iodide and bromide anions with ozone: evidence for stepwise and reversible reactions. *Phys. Chem. Chem. Phys.* **2020,** *22* (18), 9982-9989.
4. Glendening, E. D.; Landis, C. R.; Weinhold, F., NBO 7.0: New vistas in localized and delocalized chemical bonding theory. *J. Comput. Chem.* **2019,** *40* (25), 2234-2241.
5. Gottlieb, H. E.; Kotlyar, V.; Nudelman, A., NMR Chemical Shifts of Common Laboratory Solvents as Trace Impurities. *J. Org. Chem.* **1997,** *62* (21), 7512-7515.
6. Thomas, A. V., Diphenyl Phosphorazidate. In *Encyclopedia of Reagents for Organic Synthesis*, John Wiley & Sons, Ltd: 2001.
7. Armarego, W. L. F.; Chai, C. L. L., *Purification of Laboratory Chemicals*. 6 ed.; Elsevier: Oxford, Vol. 6.
8. Eaton, P. E.; Nordari, N.; Tsanaktsidis, J.; Upadhyaya, S. P., Barton Decarboxylation of Cubane-1,4-dicarboxylic Acid: Optimized Procedures for Cubanecarboxylic Acid and Cubane. *Synthesis* **1995,** (05), 501-502.
9. Griffiths, J. R.; Tsanaktsidis, J.; Savage, G. P.; Priefer, R., Thermochemical properties of iodinated cubane derivatives. *Thermochim. Acta* **2010,** *499* (1–2), 15-20.
10. Shioiri, T.; Ninomiya, K.; Yamada, S., Diphenylphosphoryl azide. New convenient reagent for a modified Curtius reaction and for peptide synthesis. *J. Am. Chem. Soc.* **1972,** *94* (17), 6203-6205.
11. Eaton, P. E.; Shankar, B. K. R.; Price, G. D.; Pluth, J. J.; Gilbert, E. E.; Alster, J.; Sandus, O., Synthesis of 1,4-dinitrocubane. *J. Org. Chem.* **1984,** *49* (1), 185-186.

12. Sheldrick GM. A Short History of SHELX. *Acta Cryst. Sect. A* **2008**, *64*, 112-122.
13. Farrugia LJ. WinGX suite for small-molecule single-crystal crystallography. *J. Appl. Crystallogr.* **1999**, *32*, 837-838.
14. Farrugia LJ. ORTEP-3 for Windows-a version of ORTEP-III with a Graphical User Interface (GUI). *J. Appl. Crystallogr.* **1997**, *30*, 565.